Geoscience Frontiers 14 (2023) 101586

Contents lists available at ScienceDirect

Geoscience Frontiers

journal homepage: www.elsevier.com/locate/gsf

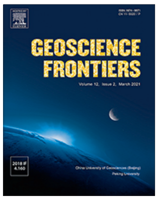

Research Paper

Cyclicity related to solar activity in lacustrine organic-rich shales and their significance to shale-oil reservoir formation

Miruo Lin[a], Kelai Xi[a,*], Yingchang Cao[a], Rukai Zhu[b], Xiaobing Niu[c], Honggang Xin[c], Weijiao Ma[a]

[a] *Key Laboratory of Deep Oil and Gas, China University of Petroleum (East China), Qingdao 266580, China*
[b] *Research Institute of Petroleum Exploration and Development, PetroChina, Beijing 100083, China*
[c] *PetroChina Changqing Oilfield Company, Xi'an 700018, China*

ARTICLE INFO

Article history:
Received 3 August 2022
Revised 3 February 2023
Accepted 15 March 2023
Available online 21 March 2023
Handling Editor: X.Q. Wan

Keywords:
Triassic
Lacustrine shales
Solar activity
Lake-level fluctuation
Shale-oil exploration

ABSTRACT

The formation mechanism of micron- to centimeter-scale sedimentary cycles in lacustrine shales is a hot topic of research, because these small-scale sedimentary cycles significantly influence shale-oil distribution heterogeneity. High-frequency paleoenvironmental evolution is an important controlling factor for the formation of small-scale sedimentary cycles. However, the driving factors of high-frequency paleoenvironmental evolution and the formation process of sedimentary cycles under its constraint remain speculative. In this study, which focuses on lacustrine shales, we find that the alternating deposition of variable thickness of organic-rich lamina (ORL) and silty-grained felsic lamina (SSFL) form sedimentary cycles on the micron to centimeter scale in the Chang 7_3 sub-member of the Yanchang Formation in the Ordos Basin. Based on detailed petrographic characterization, in-situ geochemical parameter testing, and high-resolution cycle analysis, the formation process of cyclical sedimentary records and related paleoenvironmental evolution are investigated. Three solar activity cycles were identified from the shales, namely the 360–500 yr, 81–110 yr, and 30–57 yr cycles (cycles I, II, and III, respectively). High-frequency paleoenvironmental evolution caused by solar activity induced lake-level fluctuation, which further controlled silty-grained sediment deposition and organic matter preservation in deep lake areas. Cycle I controlled relatively long-term lake-level fluctuation, driving several pairs of SSFL and ORL deposition at the centimeter scale. Cycles II and III were short-term cycles and acted on the millimeter to micrometer scale, further complicating the sedimentary strata forming during the period of lake-level fall induced by cycle I. The cyclic deposition of SSFL and ORL correspond to cycle III. Lake-level fluctuation influenced by cycle II mainly caused SSFL thickness variation in each lamina couplet. During the period of lake-level rise induced by cycle I, periods of lake level rise during cycles II, and III show cyclic variation in reducibility, and are not thought to control the supply of coarse-grained sediments in to the deep lake areas. Frequent lake-level fluctuation promotes lamina couplet formation in thickly-bedded shales, which creates favorable conditions for shale-oil accumulation. Oil produced from ORL can migrate-locally into dissolved feldspar porosity in SSFL and therefore is able to accumulate in shales, which creates high potential for future oil exploration in thickly-bedded lacustrine shales.

1. Introduction

Marine and lacustrine fine-grained sediments are excellent archives of paleoenvironmental evolution (Ilyashuk et al., 2009; Liang et al., 2018). Cyclical sedimentary records are commonly considered to be the result of periodic paleoenvironmental evolution (Anderson and Dean, 1988; Clausing and Boy, 2000; Andrews et al., 2010; Natalicchio et al., 2019; Tian et al., 2021). In comparison with marine basins, the smaller size and proximity to provenance areas means that lacustrine basins are more sensitive to paleoenvironmental evolution (Stanley, 1983; Martínek et al., 2006; Martín-Puertas et al., 2011; Huang et al., 2018). With the exception of meter-scale sedimentary cycles recording Milankovitch cycles, cyclical sedimentary records on the micron to centimeter scales can be identified in lacustrine sediments (Ripepe et al., 1991; Shunk et al., 2009; Andrews et al., 2010; Xu et al., 2019; Walters et al., 2020). These small-scale cyclical sedimentary records are mainly characterized by the alternating deposition of lamina and cyclic variations in lamina thickness, thereby recording

---

* Corresponding author.
E-mail address: xikelai@upc.edu.cn (K. Xi).

https://doi.org/10.1016/j.gsf.2023.101586
1674-9871/

high-frequency paleoenvironmental evolution at interannual to centennial timescales (Cooper et al., 2000; Park and Fürsich, 2001; Shunk et al., 2009; Park, 2017; Ma et al., 2022). There is a consensus regarding paleoenvironmental evolution and the formation mechanism of sedimentary cycles under Milankovitch-cycle constraints (Olsen and Kent, 1996; Steenbrink et al., 2003; Martínek et al., 2006; Valero et al., 2014; Percival et al., 2017). However, high-frequency paleoenvironmental evolution on interannual to centennial scales is not yet fully understood and its driving factors remain unclear (Park et al., 2001; Andrews et al., 2010; Shi et al., 2021).

Since the shale-oil revolution (Mănescu and Nuno, 2015), substantial research has focused on the understanding of shale as an oil reservoir (Jarvie, 2012; Kilian, 2016). Laminated lacustrine shales are considered favorable targets for shale-oil exploration and exploitation (Pollastro, 2007; Speight, 2012; Zhao et al., 2020). Shale can both generate oil and act as an oil reservoir (Zou et al., 2019). Different types of lamina play different roles in hydrocarbon generation and accumulation (Wilhelms et al., 1989; Liang et al., 2018; Song et al., 2020). Lamina in shales are characterized by different petrofabrics, which determine shale-oil distribution heterogeneity and can act to hinder shale-oil exploration (Washburn et al., 2015; Saif et al., 2017; Borrok et al., 2019). Researching the formation mechanism of sedimentary cycles on micron to centimeter scales may provide important insights into reserve evaluation and shale-oil exploration-target prediction (Makeen et al., 2019; Zou et al., 2019; Jin et al., 2021). Therefore, the characteristics of high-frequency paleoenvironmental evolution and related cyclical sedimentary records need to be clarified.

According to current meteorological observations, the cyclic variation in sunspot numbers generally corresponds with temperature and precipitation changes on interannual to centennial timescales (Reid, 2000; Carslaw et al., 2002). This indicates that solar activity is likely to be an important driving factor of high-frequency climate fluctuation. However, the distribution of sunspot numbers can only be reconstructed covering the past 11,400 years (Solanki et al., 2004). Therefore, previous researchers have attempted to identify possible solar activity cycles according to cyclical variations in varve thickness or grayscale (Schaaf and Thurow, 1998; Lückge et al., 2001; Vonrad et al., 2002; Andrews et al., 2010; Galloway et al., 2013).

Modern observational records show that short-term climate changes, even during a single year, can lead to marked changes in the character and volume of sediment input (Chu et al., 2005). In pre-Holocene strata, many researchers define a varve as a stable lamina couplet formed by two types of lamina with micron-scale thickness (Andrews et al., 2010; Li et al., 2018a). Microscopic measurements have been conducted to obtain the varve thickness and timescales of varve cycles (Shi et al., 2021). Some researchers have obtained the timescales of grayscale cycles by dividing the thickness of the grayscale cycle by sedimentation rates (Ma et al., 2022). Timescales of varve and grayscale cycles have been matched with the theoretical timescales of solar activity cycles to estimate whether solar activity cycles were recorded in pre-Holocene strata. Using these methods, fine-grained sediments in pre-Holocene strata, such as Cretaceous marine shales in North America (Ma et al., 2022) and Devonian lacustrine shales in northern Scotland (Andrews et al., 2010) have been shown to record solar activity signals. However, multiple solutions may occur when determining the driving factor using only timescale correspondence. The determination of the characteristics and mechanism of high-frequency paleoenvironmental evolution lacks direct evidence. Lamina are the basic unit of cyclical sedimentary records at the micron to centimeter scales (Cooper et al., 2000; Park et al., 2001). Previous research discussed the formation process of cyclical sedimentary records by analyzing the sedimentary origin of the lamina (Gabbott et al., 2010; Schieber et al., 2010; Tombo et al., 2015; Boulesteix et al., 2019; Peng, 2020), the interpretation of the development of lamina under paleoenvironment constraints remains speculative (Hughen et al., 1996; Cooper et al., 2000; Kuehn et al., 2014; Li et al., 2018a).

In the Chang 7_3 sub-member of the Ordos Basin, thickly-bedded shales deposited in deep-lake areas form excellent 'tape-recorders' for small-scale cyclical sedimentary-record identification and high-frequency paleoenvironmental reconstruction. This study uses petrographical analysis and in-situ geochemical testing to (1) characterize cyclical sedimentary records in thickly-bedded shales at the micron to centimeter scale, (2) clarify the mechanism of high-frequency paleoenvironmental evolution and related cyclical sedimentary records in lacustrine basins, and (3) discuss the significance of cyclical sedimentary records on shale oil reservoir exploration and characterization.

2. Geological background

The Ordos Basin is a large multi-cycle cratonic basin located in the western North China Block (Zhang et al., 2020). It is bound to the east by the Lvliang Mountain and Lishi Fault, to the west by the Helan Mountain, to the north by the Xing'an Mongolian Orogenic Belt and the Dengkou-tuoketuo Fault, and to the south by the Qinling Orogenic Belt and Huaibei Flexure Belt (Yang et al., 2007) (Fig. 1A). Late Triassic intermediate-acidic and intermediate-basic volcanic rocks developed in the southern and western Qinling Orogenic Belts, respectively (Fig. 1A, B).

During the deposition of the Triassic Yanchang Formation, which was affected by the Indosinian Orogeny, a large-scale inland-depression lake basin formed (Fu et al., 2018, 2020). During this period, a set of terrigenous clastic rocks of mainly fluvial-lacustrine facies were deposited in the basin. They are divided into 10 members, namely Chang 1 to 10 (Fu et al., 2020). The Chang 7 member is divided into three sub-members, namely Chang 7_1, Chang 7_2, and Chang 7_3. The studied Chang 7_3 sub-member, with a thickness of 28–42 m, is a shale-dominated formation at a burial depth of 1500–3000 m (Fig. 1B, C) and was deposited in warm and humid conditions (Yang et al., 2010). At that time, the highest lake level was reached, forming a large deep-lake area in the Ordos Basin (Fu et al., 2020). The observed thinly-bedded sandstones of gravity flow origin and the thickly-bedded shales mainly deposited in the deep-lake area (Liu et al., 2021). According to the lithological description, the gravity flow sandstones mainly occur at the top and bottom of the Chang 7_3 sub-member, while the thickly-bedded shales are deposited between them (Fig. 1D). Several tuff layers, with a thickness of 5–17 mm, were identified in the thickly-bedded shale interval (Fig. 1D). In order to eliminate the interference of thickly-bedded slump and flood deposits on cyclostratigraphy research (rapid changes in sedimentary rates significantly affect the results of spectral analyses) (Hinnov, 2000), thickly-bedded shales that reflect the continuous deep-water environment were selected as the focus interval for this study.

Based on the zircon U–Pb dating of tuff layers, the thickly-bedded shales in the Chang 7_3 sub-member began to deposit at 233.2 Ma (Fig. 1D) (Lu et al., 2021), confirming that the thickly-bedded shales were deposited during the Carnian Pluvial Event (CPE) in the late Triassic (Preto et al., 2010; Corso et al., 2018). During this period, the Ordos Basin was located in eastern Tethys in approximately middle latitudes of the northern hemisphere (Fig. 1A) (Carroll et al., 2010). The CPE triggered a global humid climate, accompanied by a rise in temperature and an increase in rainfall, which induced the increased run-off and facilitate the siliciclastic sediment transport to the lake basin (Dal Corso et al.,

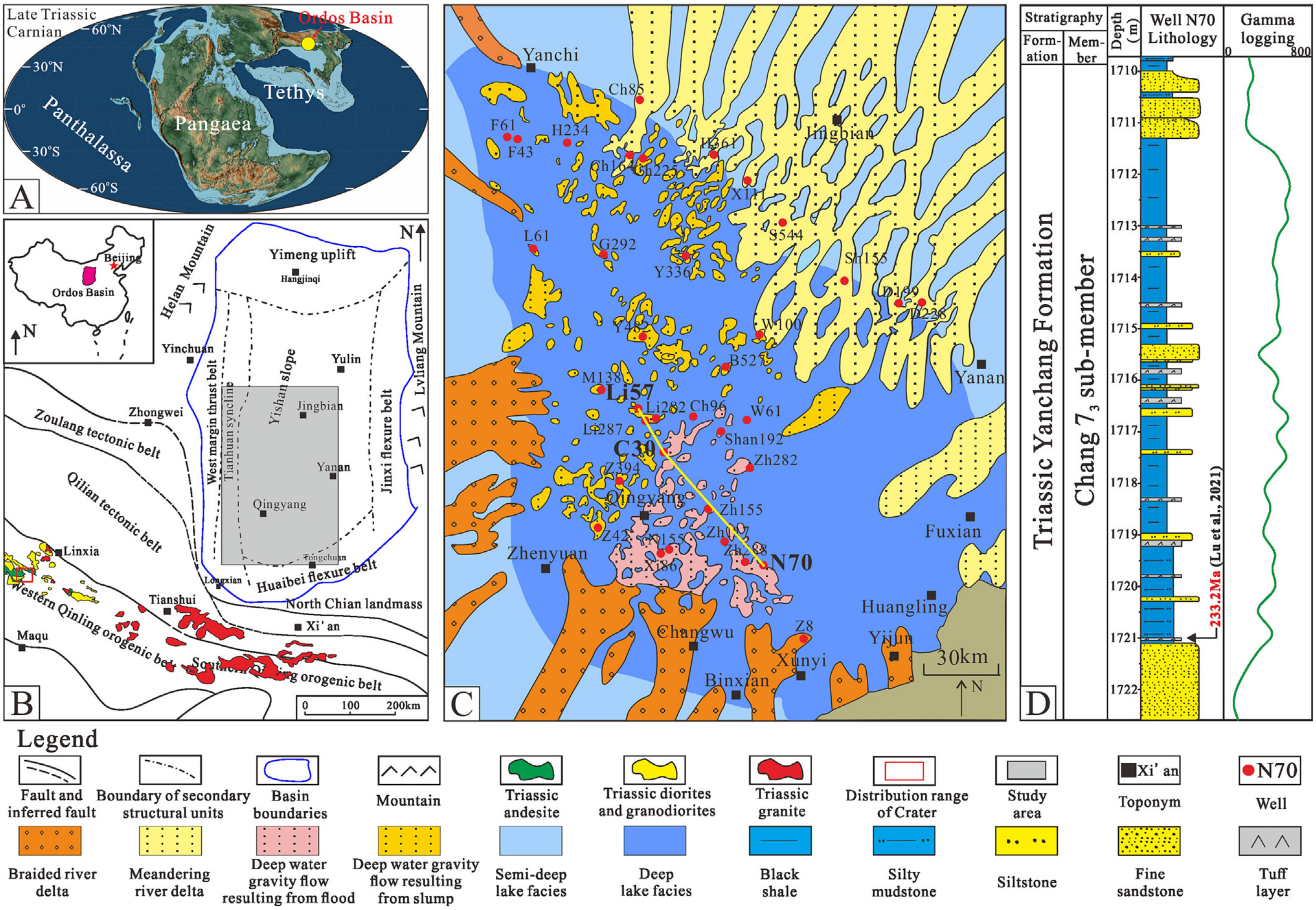

Fig. 1. (A) Palaeogeographic map of the late Triassic (Scotese, 2014) and the location of the Ordos Basin during the late Triassic. (B) Tectonic location of the Ordos basin showing distribution of uplifts, flexure belts and orogenic belts (Zhou et al., 1995; Fu et al., 2018). (C) Plane distribution characteristics of sedimentary facies and well sites in Chang 7_3 sub-member. (D) Stratigraphic development characteristics, including the zircon U-Pb dating result of tuff layer, in Chang 7_3 sub-member.

2020). On this basis, the parent rocks in north-eastern and south-western provenances, as well as tephra sourced from the Qinling Orogenic Belt would provide abundant sediments into the Ordos Basin (Yang et al., 2010; Wang et al., 2013; Wang et al., 2017a). Under the warm and humid paleoclimate, a strongly reducing environment also led to the deposition and preservation of organic-rich shales (Yang et al., 2010; Zhang et al., 2016). Total organic carbon (TOC) in thickly-bedded shales varies from 5.33% to 30.69%, with an average of 18.3%, and kerogens are mainly humic and sapropelic types (Yang et al., 2010; Fu et al., 2019). The deposition of thickly-bedded organic-rich shales in the Chang 7_3 sub-member provided favorable conditions for reservoir formation and shale-oil accumulation (Fu et al., 2020).

3. Database and methods

Three boreholes (N70, C30, and Li57) through the Chang 7_3 sub-member in the Ordos Basin were selected for analysis. Bulk shale samples were collected from the three key boreholes. Shale samples were prepared for thin sectioning and microscope observations. Typical samples with clear and relatively flat lamina interfaces were selected for advanced mineral identification and characterization system (AMICS) analyses. Bulk shale samples with clear lamination structures were polished and underwent micro-X-ray fluorescence spectroscopy (Micro-XRF) analysis. In order to obtain organic geochemical data from different lamina, shale samples with clear lamina interfaces and of sufficient thicknesses were chosen for microdrilling. Dispersed framboidal pyrite minerals in the organic-rich lamina (ORL) and adjacent silty-grained felsic lamina (SSFL) from wells N70 and C30 were selected for in situ S-isotope testing by laser-ablation multi-collector inductively coupled plasma-mass spectrometry (LA-MC-ICP-MS).

3.1. Petrographic analysis

Microscopic observations focused on lamina type, thickness, and distribution, as well as the grain size of the framboidal pyrites. This petrographical analysis was performed using a 'Zeiss microscope' (Imaging-2 M). Quantitative statistics of the mineral compositions in different lamina types were calculated using an AMICS analysis using a scanning electron microscope (Zeiss Crossbeam 550 FIB-SEM) integrated with a Bruker EDS analysis system (X-Flasher Detector 430-M). Thin sections were carbon-coated and glued onto aluminum stubs. During AMICS analysis, the area was first scanned using backscattering (BSE), followed by automatic mineral identification using high-resolution energy-dispersive X-ray spectrometry (EDS). AMICS analysis software and databases were used for identifying mineral boundaries that were resolvable up to 20 μm. The microscopic observations, SEM-BSE observations, and AMICS analyses were performed at the Key Laboratory of Deep Oil and Gas, China University of Petroleum (East China).

3.2. Geochemical analysis

A Micro-XRF analysis was used to identify cyclical sedimentary records in shales through continuous in-situ element testing of bulk core samples. This was conducted using a ‘Bruker M4 Tornado’ high-performance XRF spectrometer, with each sample being polished to enhance the image resolution. The samples were placed in the sample compartment and aligned horizontally using a level gauge. Element scanning was performed using a silicon drift detector, with an acceleration voltage of 50 keV and beam current of 800 mA. Rhodium was chosen as the target material for the X-ray irradiation, and the scanning rate was ~ 30 ms/point. The quantitative characteristics of Na, K, Ca, Mg, Al, Si, Fe, S, Mn, Sr, Ti, V, Cr, Cu, Ni, Co, Sr, Ba, and Mo were determined for each sample. Each bulk shale sample (~10 cm in length and width) was scanned for > 8 h. The analytical accuracy was 20 μm. Element concentrations were reported in wt.%. An element distribution map was used for analyzing the lamina types and the distribution of different lamina in the core samples. Due to the variety of element-enrichment characteristics in different lamina, the lamina in the image exhibited different colors after element stacking. Different types of lamina in the micro-XRF analysis images were calibrated based on microscopic observations. Finally, multi-scale cyclical sedimentary records were determined by identifying the distribution characteristics of different types of lamina in the micro-XRF images. After an elemental analysis of the bulk shale samples, a rectangular area perpendicular to the lamina was selected in each sample, from which quantitative analysis results were extracted. The scanning spacing perpendicular to the lamina was approximately 35 μm. Geochemical parameters, including the Mo/Ti ratio and C value, were analyzed to reconstruct the high-frequency paleoenvironmental evolution. The increase and decrease in the Mo/Ti ratio reflect the enhancement and reduction of reducibility, respectively (Brucker et al., 2011). Mo/Ti ratio reflects the ratio of Mo to Ti content. The increase and decrease in C values reflect enhancement and reduction of humidity, respectively (Qiu et al., 2015). The C value = Σ (Fe + Mn + Cr + Ni + V + Co)/Σ (Ca + Mg + K + Na + Sr + Ba), where each element in the formula represents the content of the corresponding element.

Micro-drilling powders were used for Rock-Eval analysis, kerogen/hydrocarbon extraction, gas chromatography–mass spectrometry (GC–MS) analysis, and carbon-isotope analysis of kerogen. Micro-drilling was conducted using a micro drill system (Marathon BM50M), with a drill diameter of 100 μm. The bulk shale samples were polished to better distinguish the different types of laminae under a standard optical microscope. Using the ‘Elab-TOC’, Rock-Eval analysis was conducted on the powders drilled from different lamina to analyze the TOC. For kerogen extraction and carbon-isotope analysis, a microdrilling sample of approximately 1.0 g was extracted from each selected area, and 6–12 mg of kerogen was extracted per sample. The kerogens were acid-washed with 10% HCl and neutralized with deionized water, then weighed into tin capsules and wrapped. The $\delta^{13}C_{org}$ content within the kerogen was measured using a stable isotope mass spectrometer (ThermoFinigan Delta Plus XL) with a precision better than ± 0.1 ‰. The carbon isotope values are given in per mille relative to VPDB. For hydrocarbon extraction and GC–MS analysis, the powders were added into solvent [Dichloromethane: Methanol (93:7, v: v)] and stirred with a glass stick. After ultrasonic shock for 10 min, quiescence of the solution in room temperature was maintained for 24 h. Repeat the above steps until the solvent volatilizes to obtain extracted organic matter. All expelled saturated hydrocarbons were following analyzed for GC–MS by Agilent 5977B GC/MSD. Helium was used as the carrier gas and the injector temperature was 300 ℃. The temperature of GC oven was initially set at 50 ℃, and programmed to 120 ℃ at 20 ℃/min, then to 310 ℃ at 3 ℃/min with a final hold of 25 min. The mass spectrometer was operated in full scan mode with a scan range of 50–600 Da. An in-situ sulfur-isotope analysis of pyrite was used to determine the evolution of the paleo-redox conditions within the water column during the deposition periods of the different types of lamina. This was conducted using a ‘Nu Plasma 1700 LA-MC-ICP-MS’, which is a 193 nm excimer-laser denudation system (RESOlution m-50, ASI), with a fluence of laser energy of 3.6 J/cm^2, frequency of 3 Hz, spot size of 25 μm, single-point denudation, high-purity helium carrier gas (280 mL/min), and argon (Ar) supplement gas (0.86 L/min). The S isotopic composition was expressed as a relative value:

$$\delta^{34}S = \left[\left({}^{34}S/{}^{32}S_{\text{sample}}\right)/\left({}^{34}S/{}^{32}S_{\text{standard}}\right) - 1\right] \times 1000$$

IAEA-S-1 (Ag_2S; $\delta^{34}S_{\text{V-CDT}} = -0.3‰$) was used as the standard sample. The laboratory standards of S isotopes were determined by using gas stable-isotope mass spectrometry or the SOLUTION injection MC-ICP-MS method, and the standard samples used in the determination were IAEA-S-1, IAEA-S-2, and IAEA-S-3 (Ag_2S powder) (Bao et al., 2017; Chen et al., 2017).

The micro-XRF analysis, micro-drilling, Rock-Eval analysis, and GC–MS analysis were performed at the Key Laboratory of Deep Oil and Gas, China University of Petroleum (East China). The in-situ sulfur-isotope analysis of pyrites was conducted at the State Key Laboratory of Continental Dynamics, Northwest University, China. Kerogen extraction and carbon-isotope analyses were performed at the Guangzhou Institute of Geochemistry, Chinese Academy of Sciences (CAS).

3.3. Time series analysis

The geochemical parameters obtained from the micro-XRF analysis were de-trended using the Past software (Hammer et al., 2001). The Redfit software was then used to perform a spectral analysis, which was based on Fourier transform of the preprocessed data (Schulz and Mudelsee, 2002). The frequencies of the statistically significant peaks (with confidence over 90%) were determined. Through this, the stratigraphic thicknesses of cycles were determined within the Chang 7_3 sub-member. Repeating the procedure outlined above for all samples, this study identified the thickness of stratigraphic cycles within the datasets. A Multitaper method of spectral analysis (MTM analysis) and a wavelet analysis, which is based on induction logging curves, was performed on thickly-bedded shales from Well N70 to identify potential Milankovitch cycles within the dataset. Subsequently, the sedimentation rates of the thickly-bedded shale were obtained using the correlation-coefficient method (COCO/eCOCO) of the ‘Acycle 2.3’ software (Li et al., 2018b). The timescale of each stratigraphic cycle was obtained by dividing the thickness of the stratigraphic cycles by the corresponding sedimentation rates. These timescales were used for analyzing the driving factors of paleoenvironmental evolution. The obtained cycle thicknesses underwent filtering analysis using the Gaussian filter in ‘MATLAB2019’ software.

4. Results

4.1. Petrological characteristics in laminated lacustrine shales

Lamina structures are developed mainly in organic-rich shales in the Chang 7_3 sub-member. Two types of lamina can generally be identified, namely, organic-rich lamina (ORL) and silty-grained felsic lamina (SSFL) (Fig. 2A). Silty-grained K-feldspar, plagioclase, and quartz are dominant in the SSFL (Fig. 2B, D). The K-feldspar content is approximately 70% and the plagioclase and quartz content are approximately 7.24% and 5.53%, respectively (Fig. 2B, D).

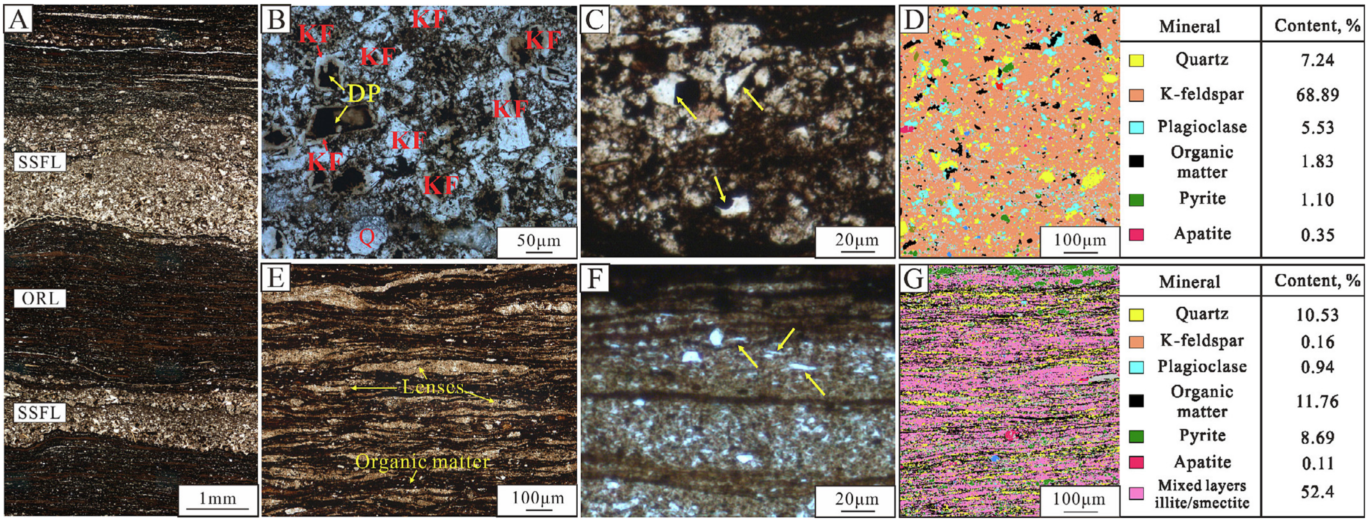

	Mineral	Content, %
🟨	Quartz	7.24
🟧	K-feldspar	68.89
🟦	Plagioclase	5.53
⬛	Organic matter	1.83
🟩	Pyrite	1.10
🟥	Apatite	0.35

	Mineral	Content, %
🟨	Quartz	10.53
🟧	K-feldspar	0.16
🟦	Plagioclase	0.94
⬛	Organic matter	11.76
🟩	Pyrite	8.69
🟥	Apatite	0.11
🟪	Mixed layers illite/smectite	52.4

Fig. 2. Petrological characteristics of lacustrine shales in Chang 7_3 sub-member. (A) Well C30, 1964.88 m, with petrographic images of ORL and SSFL under plane-polarized light. (B) Well C30, 1964.88 m, showing mineral characteristics and dissolution pores in SSFL under plane-polarized light. (C) Well C30, 1964.88 m, showing grains with angular boundaries in SSFL under plane-polarized light. (D) Well C30, 1964.88 m, showing AMICS analysis results of SSFL. (E) Well C30, 1968.32 m, showing lenses rich in clay mineral and organic matter in ORL under plane-polarized light. (F) Well N70, 1711.80 m, showing small amounts of feldspars in ORL under plane-polarized light. (G) Well C30, 1964.88 m, showing AMICS analysis results of ORL. KF – K-feldspar, Q – quartz, DP – dissolution pore, SSFL – silty-grained felsic lamina, and ORL – organic-rich lamina.

Mixed-layer illite/smectite, organic matter, and pyrite are dominant in the ORL, at approximately 52%, 12%, and 9%, respectively (Fig. 2G). Small amounts of silty-grained feldspars are observed within the ORL (Fig. 2G). Abundant intra-granular dissolution porosity is observed to develop within the feldspars (Fig. 2B). Grains with sharp angles are commonly distributed in the SSFL (Fig. 2C). Most of the silt-sized grains display A-axis alignment (Fig. 3A). Grain sizes in the SSFL range from 10 to 110 µm, which are clustered between 20 µm and 80 µm (Fig. 3B).

Laminated shales are formed by the cyclic deposition of two types of lamina (SSFL and ORL) (Fig. 3A). Fining-upward SSFL and water-escape structures are evident in laminated shales (Fig. 3A,

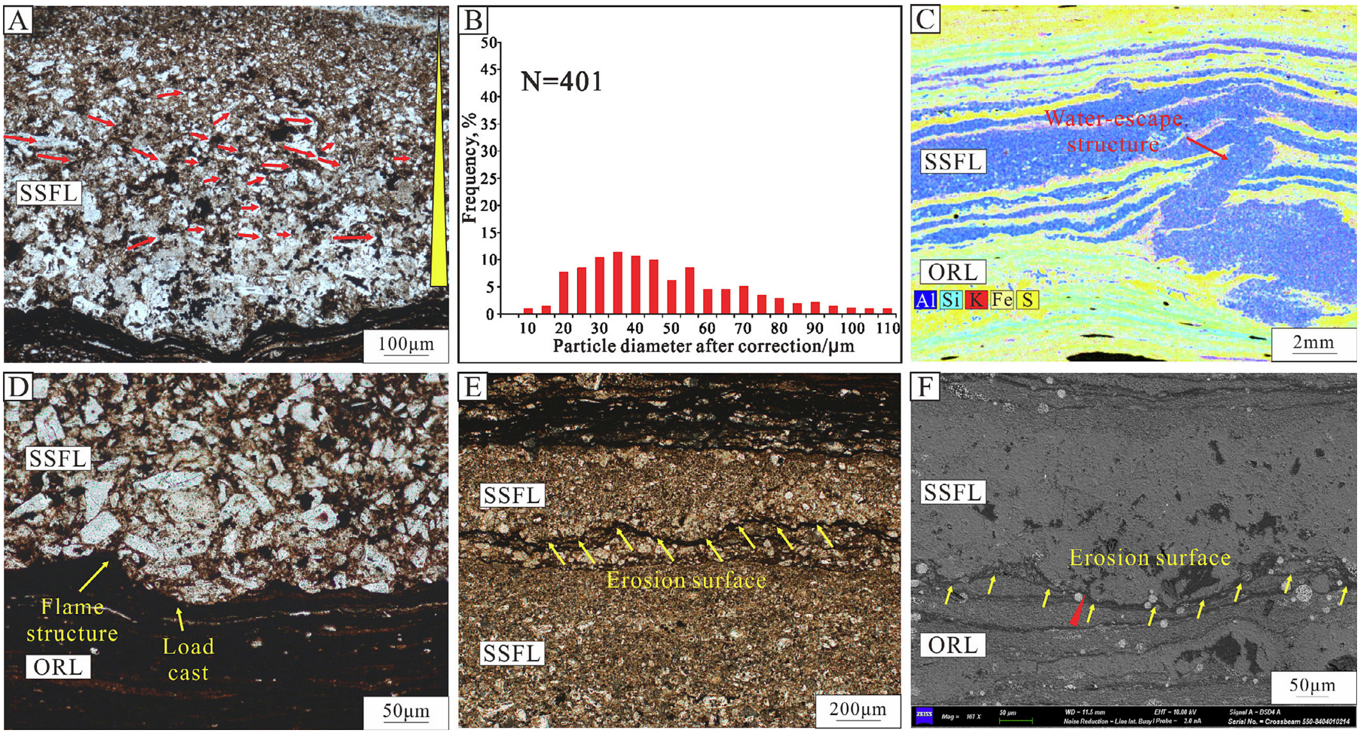

Fig. 3. Characteristics of typical sedimentary structures in SSFL. (A) Well Z8, 1277.22 m, showing fining upwards SSFL under plane-polarized light. Red arrow indicates the long axis of the grains. (B) Well Z8, 1277.22 m, showing grain size distribution in the SSFL obtained in thin sections. (C) Well C30, 1967.30 m, showing water-escapes structure in SSFL, identified in a Micro-XRF image. (D) Well Li57, 2348.34 m, showing load casts and flame structures preserved at the bottom of SSFL, under plane-polarized light. (E) Well Z8, 1282.85 m, showing erosion surfaces preserved at the bottom of SSFL, under plane-polarized light. (F) Well N70, 1718.90 m, showing an erosion surface preserved at the bottom of SSFL under SEM. Red triangle indicates where the organic matter is eroded by SSFL. SSFL – silty-grained felsic lamina, and ORL – organic-rich lamina. (For interpretation of the references to colour in this figure legend, the reader is referred to the web version of this article.)

C). Erosion surfaces and load casts also occur at the bottom of the SSFL (Fig. 3D, E, and F). Clay minerals and organic matter in the ORL are generally squeezed upward into the load cast, forming a flame structure (Fig. 3D). The organic matter debris in the ORL is significantly eroded by the SSFL (Fig. 3F). Lenticular fabric is developed in the ORL (Fig. 2E). Individual lenses are up to several hundred micrometers in length (Fig. 2E). Abundant lenses of mixed-layer illite/smectite, are stratified and alternately deposited with organic matter (Fig. 2E). Nowadays, it is generally believed that fine-grained sediments are usually deposited by suspension in deep-lake area (Alçiçek et al., 2007; Tänavsuu-Milkeviciene and Frederick Sarg, 2012; Liang et al., 2018). However, the discovery of microstructures shows that the suspension settling cannot explain the sedimentary process of the two types of laminae in the deep-lake area of the Ordos Basin. Microstructures such as load cast (Fig. 3D), water-escape structures (Fig. 3C), and erosion surfaces (Fig. 3E–F) in fining-upward SSFL demonstrated that silty-grained sediments were transported by low-density turbidity currents (Stow and Shanmugam, 1980; Ayranci et al., 2018; Boulesteix et al., 2019). The identification of lenticular fabric in ORL indicate the clay-grained sediments were also deposited in the dynamic depositional condition (Schieber et al., 2010; Könitzer et al., 2014). However, the obvious reduction of silty-grained sediments content suggests that the hydrodynamic conditions during ORL deposition are weaker than SSFL (Baas et al., 2016, 2021).

From the edge to the center of the Ordos Basin, the water depth gradually increases and the frequency and thickness and grain size of SSFL show high variation (Fig. 4). In the area close to the southern edge of the Ordos Basin (Well N70), the thickness and frequency of the SSFL ranges from 0.41 to 1.75 mm and from 9.69% to 22.72%, respectively (Fig. 4A). The grain size in the thickest of the SSFL in Well N70 primarily range from 50.28 to 89.50 μm (Fig. 4B). The SSFL is observed almost exclusively within the thickly-bedded shale interval in Well N70, and its thickness generally shows a cyclic variation (Supplementary Data Fig. S1). In the area close to the center of the Ordos Basin (wells C30 and Li57), the thickness and frequency of the SSFL decreases from proximal to distal palaeo-lake basin (Fig. 4). The grain sizes in the thickest of the SSFL in wells C30 and Li57 range from 30.01 to 59.80 μm and from 10.07 to 29.82 μm, respectively (Fig. 4B). The SSFL mainly develops in the low part of the thickly-bedded shale interval, and there is strongly-observed cyclicity within the SSFL thicknesses adjacent to the center of the Ordos Basin (Supplementary Data Fig. S1).

4.2. Element distribution in lacustrine shales

The element types and abundances clearly differ in the SSFL and ORL. Al, Si, and K are concentrated in the SSFL and Fe, Mo, and Cu are abundant in the ORL (Fig. 5A). In a single SSFL, the Al, Si, K, Fe, Mo, and Cu content exhibited no significant fluctuation. In a single ORL, the Al, Si, and K content show almost no significant change in the vertical direction (Fig. 5B–D). Fe, Mo, and Cu are relatively enriched in the middle part of the ORL and gradually decrease with decreasing distance from the SSFL deposited on the either side of the ORL (Fig. 5E–G). The lamina couplet thickness in shale is commonly at the micron to millimeter scale (Fig. 5). This results in the cyclic distribution of Fe, Mo, and Cu content at these small scales. The Mo/Ti ratio and C value correlate well with the Mo, Fe, and Cu content (Fig. 5E–I), indicating that cyclic variations in the redox indicators and humidity are recorded at the micron to centimeter scale.

4.3. Cyclical variations of geochemical parameters on thickness and timescales

A Fourier-transform spectrum analysis was used to identify possible cycles of paleoenvironmental evolution based on the quantitative results of the Mo/Ti ratio and C value. In thickly-bedded shales from Well N70, three cycles of stable existence were identified. The thicknesses of these three stratigraphic cycles were 18.0–26.7, 3.6–5.9, and 1.5–2.8 mm (Supplementary Data Figs. S2 and S3). The sedimentation rates of the thickly-bedded shales were obtained through identification of the Milankovitch cycles. A multitaper method of spectral analysis (MTM analysis) based on induction logging curves was used. The thickness ratio of the stratigraphic cycles, with a confidence coefficient > 90% in the MTM analysis, was 4.85 m: 2.42 m: 1.94 m: 1.10 m: 0.94 m, which shows the ratio feature of 5.139: 2.569: 2.056: 1.171: 1.000 (Fig. 6A). This matches with published theoretical period ratios of orbit parameters (5.362-eccentricity: 2.560-obliquity: 2.015-obliquity: 1.195-precession: 1.000-precession) during the late Triassic (Berger et al., 1989). The wavelet analysis also confirms that the thickness of these stratigraphic cycles underwent no significant changes during the period of shale deposition (1710.5 m–1721.1 m) (Fig. 6B). Therefore, the eccentricity, obliquity, and precession signals are interpreted as being identifiable within this data from the Chang 7_3 sub-member. Using the COCO method, and based on stable astronomical-cycle signals, the average sedimentation rate in the Chang 7_3 sub-member is estimated to be 5.4 cm/kyr (>99% confidence coefficient) (Fig. 6B), and the average sedimentation rates of 4 and 10 cm/kyr had a confidence coefficient of > 90% (Fig. 6B). Using the eCOCO method, the sedimentation rate of the thickly-bedded shales was found to be 5.4 cm/kyr (Fig. 6C). The sedimentation rate decreased to 4 cm/kyr only at the bottom of the thickly-bedded shales (Fig. 6C). Based on the identification of the Milankovitch cycles, we calculated that the sedimentation rate of the thickly-bedded shales (>10 m in thickness) in the Chang 7_3

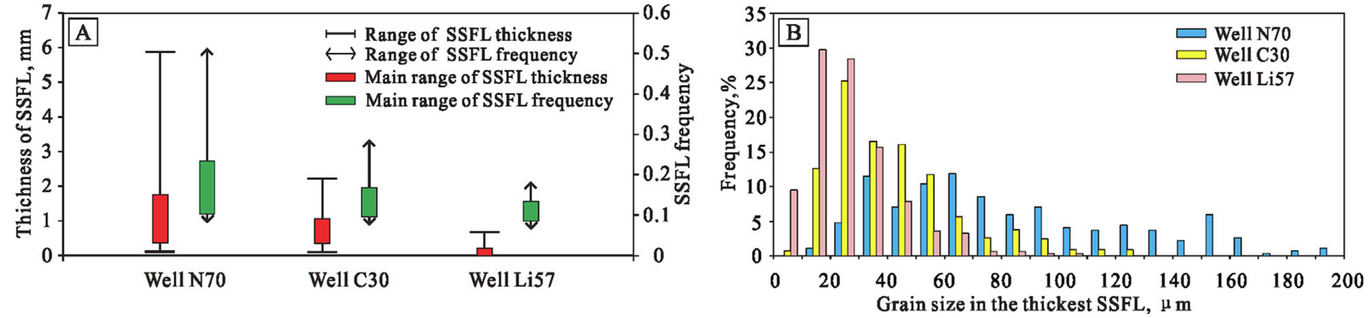

Fig. 4. Characteristics of laminar thickness, frequency, and grain size in different locations. (A) Changes of SSFL thickness and frequency in laminated shales from proximal to distal palaeo-lake basin. (B) Changes of grain size distribution in the thickest SSFL from proximal to distal palaeo-lake basin. The positions of Well N70, Well C30 and Well Li57 are shown in Fig. 1B. SSFL frequency is indicated by the number of SSFL per millimeter.

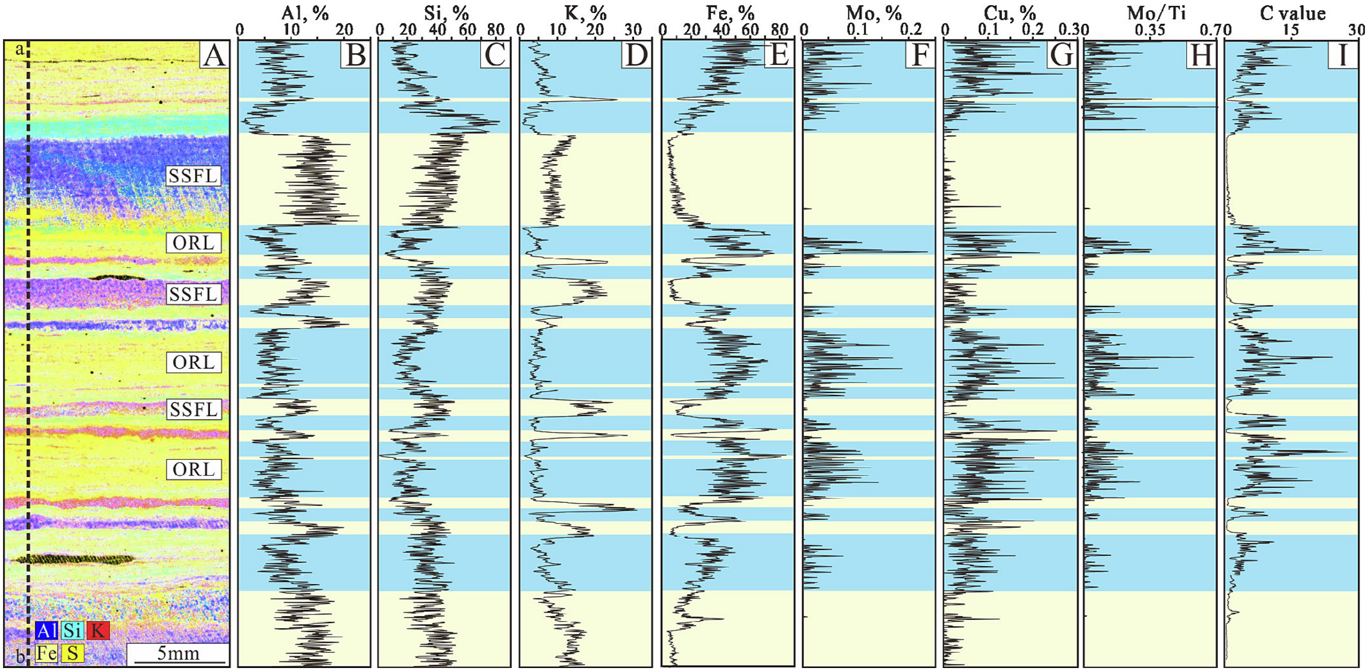

Fig. 5. Distribution characteristics of elements in SSFL and ORL in Well N70, 1719.20 m. (A) Element distribution map obtained by Micro-XRF analysis. (B–G) Element distribution characteristics in different types of laminae. (H–I) Distribution characteristics of Mo/Ti ratios and C values in different types of laminae. Blue rectangle – ORL; yellow rectangle – SSFL; SSFL – silty-grained felsic lamina; ORL – organic-rich lamina. (For interpretation of the references to colour in this figure legend, the reader is referred to the web version of this article.)

sub-member from Well N70 was 4.0–5.4 cm/kyr (Fig. 6C). Zhao et al. (2020) undertook isotope dilution thermal ionization mass spectrometry (ID-TIMS) dating for accurate zircon dating of tuffs in the Chang 7_3 sub-member, which they used for astronomical tuning, and the sedimentation rate of the thickly-bedded shales in the southern Ordos Basin was 4.0–4.9 cm/kyr. Well N70 is located in the southern Ordos Basin (Fig. 1C), and the sedimentation rate calculated in this study compares closely with that from Zhao et al. (2020). Combined with the sedimentation rate calculated in the present study, three distinct stable cycles were identified on interannual to centennial timescales in examples of the thickly-bedded shales (Fig. 7 and Table 1).

The paleoenvironmental evolution cycles of 360–500 yr, 81–110 yr, and 30–57 yr correspond exactly to sedimentary cycles on the centimeter-, millimeter-, and millimeter to micron-scales, respectively (Fig. 8). The centimeter-scale sedimentary cycle (CSR I) involves the cyclic deposition of several SSFL and ORL (Fig. 8A–B). The thickness of a single CSR I is between 2 and 3 cm, which consists of c. 10 groups of lamina couplets. The millimeter-scale sedimentary cycle (CSR II) is formed by the cyclic change of the lamina thickness in each lamina couplet (Fig. 8C). The thickness of a single CSR II ranges from 4 mm to 6 mm, which consists of approximately-three groups of lamina couplets. The millimeter-to-micron-scale sedimentary cycle (CSR III) involves alternations of SSFL and ORL (Fig. 8D). The thickness of a single CSR III ranges between 0.95 mm and 2.60 mm and is composed of one lamina couplet.

5. Discussion

5.1. Paleoenvironmental evolution and cyclical fluctuations of sedimentary records

Tectonic activity was relatively stable during the sedimentary period of the Chang 7_3 sub-member in the Ordos Basin (Fu et al., 2018), and therefore paleoclimate variation became the main factor controlling changes in the sedimentary environment. The long-held view has been that the Triassic was a stable hot-house world (Kiessling, 2010; Preto et al., 2010). Recently, the discovery of the CPE and mega-monsoonal circulation suggests that the Triassic paleo-environmental evolution was unstable (Hornung et al., 2007; Corso et al., 2018). The CPE triggered the humid paleoclimate, which lasted for approximately 1 Ma in the late Triassic, whereas the mega-monsoonal circulation commonly induced an arid-humid climatic change that lasted one year. The timescales of paleoenvironmental fluctuation caused by these two factors are clearly at odds with the timescales of the high-frequency paleoenvironmental evolution identified in this study. Regional volcanic eruptions also occurred during the late Triassic, as is indicated by the deposition and preservation of tuff layers (Fig. 1D). The minimum separation between the tuff layers is approximately 25 cm (Fig. 1D). However, we found that the paleoenvironmental evolution cycle of 360–500 yr was recorded by the sedimentary cycle in 2–3 cm of thickness. Obviously, the regional volcanism adjacent to the Ordos Basin is unlikely to be a driving factor of high-frequency paleoenvironmental evolution in this study. Although there are other volcanisms around the globe in the CPE interval (Sun et al., 2016), the kind of volcanic activity that can cause such steady and high-frequency paleoenvironmental fluctuation seems hard to occur. Therefore, we speculate that there are other factors controlling the high-frequency paleoenvironmental evolution in the Ordos Basin.

The timescale of the paleoenvironmental evolution cycle identified here is similar to that of the solar activity cycle. Classical solar activity cycles include the Schwabe (~11 yr), Hale (~22 yr), Gleissberg (~88 yr), and Suess quasi-cycles (~208 yr) (Dicke, 1979; Damon and Sonnett, 1991; Hoyt and Schatten, 1998). Furthermore, solar activity cycles were also thought to involve long-scale quasi-cycles from ~ 352 yr to ~ 2.241 kyr. These were identified using ^{14}C analysis of tree rings (Damon and Sonnett, 1991; Yin et al., 2007). Previous research has identified the effects of solar activity

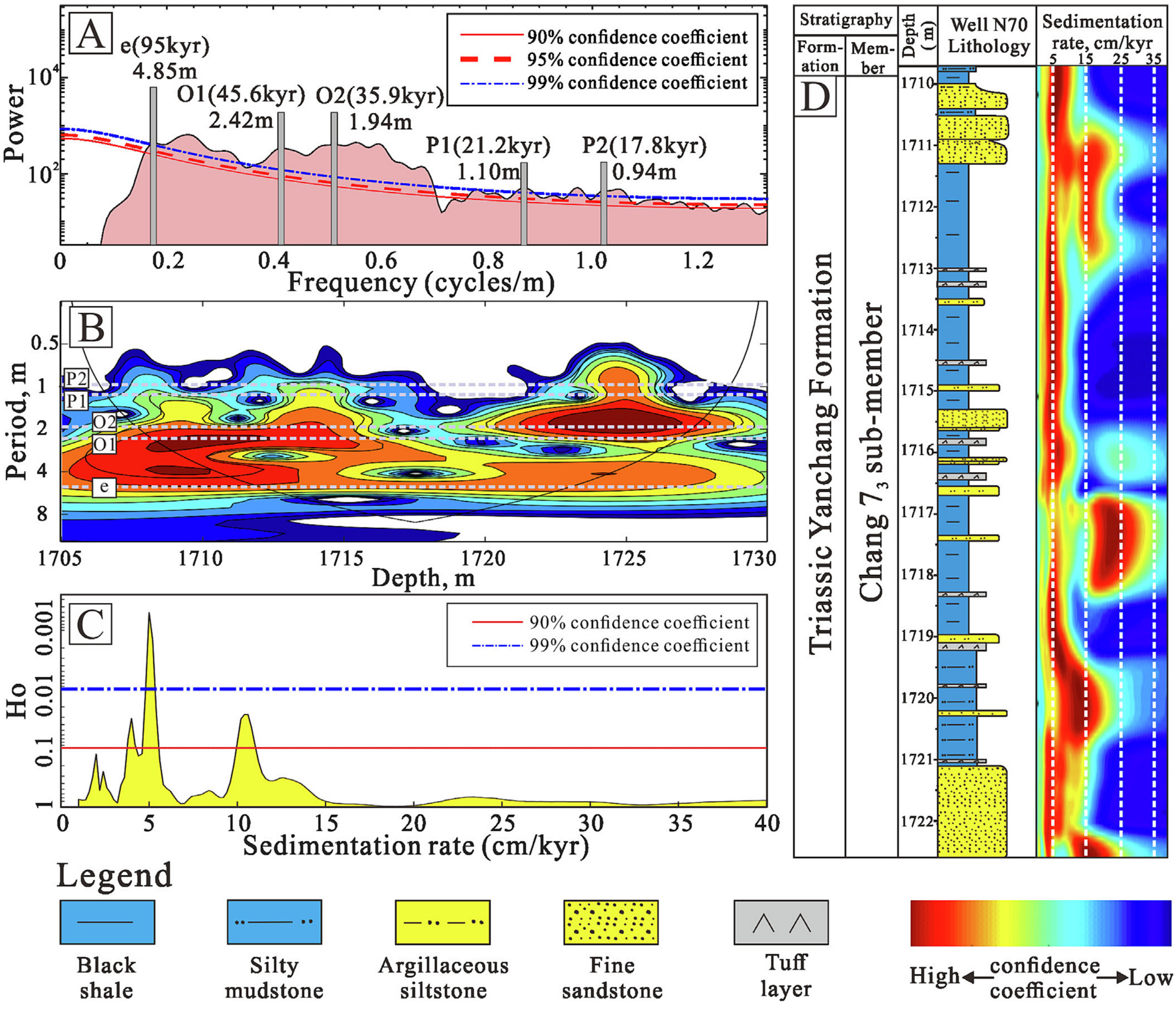

Fig. 6. Identification of Milankovitch cycles and sedimentation rate analysis in the Chang 7_3 sub-member. (A) MTM analysis based on the induction logging curve of Chang 7_3 sub-member. (B) Wavelet analysis based on the induction logging curve of Chang 7_3 sub-member. The wavelet analysis confirms that the thickness of eccentricity, obliquity, and precession cycles have no significant changes during the period of shale deposition (1710.5 m – 1721.1 m). (C) Average sedimentation rate of Chang 7_3 sub-member using the COCO method analysis. (D) Sedimentation rate of thickly-bedded shales in Chang 7_3 sub-member using eCOCO method analysis.

cycles in strata from the Mesoproterozoic to the Holocene (Ripepe et al., 1991; Heydari et al., 1997; Hughes et al., 2003; Shunk et al., 2009; Andrews et al., 2010; Ma et al., 2022). Previous research suggests that solar activity cycles and the Earth–climate interaction may have remained unchanged for the past 1.2 Ga (Milana and Lopez, 1998; Andrews et al., 2010). The 30–50 yr cycles remained stable from the Devonian to the Holocene (Anderson and Koopmans, 1963; Ernesto and Pacca, 1981; Ripepe et al., 1991; Milana and Lopez, 1998; Wang et al., 2005; Andrews et al, 2010; Galloway et al., 2013). Based on current sunspot observations, the analytical results of the variance normalized global wavelet power spectrum showed that the 30–50 yr cycle also represents the product of the solar activity cycle (Li et al., 2004; Zhao and Feng, 2014). Therefore, the stable cycles of 360–500 yr, 81–110 yr, and 30–57 yr (cycles I, II, and III, respectively) are interpreted to reflect solar activity cycles (Fig. 7).

On interannual to centennial timescales, solar activity is mainly responsible for driving climate systems (Reid, 2000; Mao et al., 2009), leading to marked periodic changes in temperatures and lake levels (Reid, 2000; Magny et al., 2010). When the number of sunspots increases, intense solar activity results in a temperature increase (Reid, 2000; Liu et al., 2019), while a stronger than usual solar magnetic field sweeps through interplanetary space, thereby shielding the Earth more effectively from cosmic rays (van Geel et al., 1999; Gray et al., 2010). A decrease in incoming cosmic rays adversely affects cloud formation, which decreases precipitation and rainfall efficiency (Kniveton and Todd, 2001; Carslaw et al., 2002; Lucio, 2005), eventually leading to an arid climate and a lake-level drop (Magny et al., 2010; Song et al., 2015; Li et al., 2018a). In contrast, when the number of sunspots decreases, weak solar activity results in a low-temperature humid climate and lake-level rise.

The lake-level fluctuation in the 360–500 yr cycle I induced centimeter-scale cyclical sedimentary records (Fig. 9A, B). The semi-cycle with $\delta^{13}C$ enrichment and lower C values represents a warm and arid paleoenvironment (Ku and Li, 1998; Paulsen

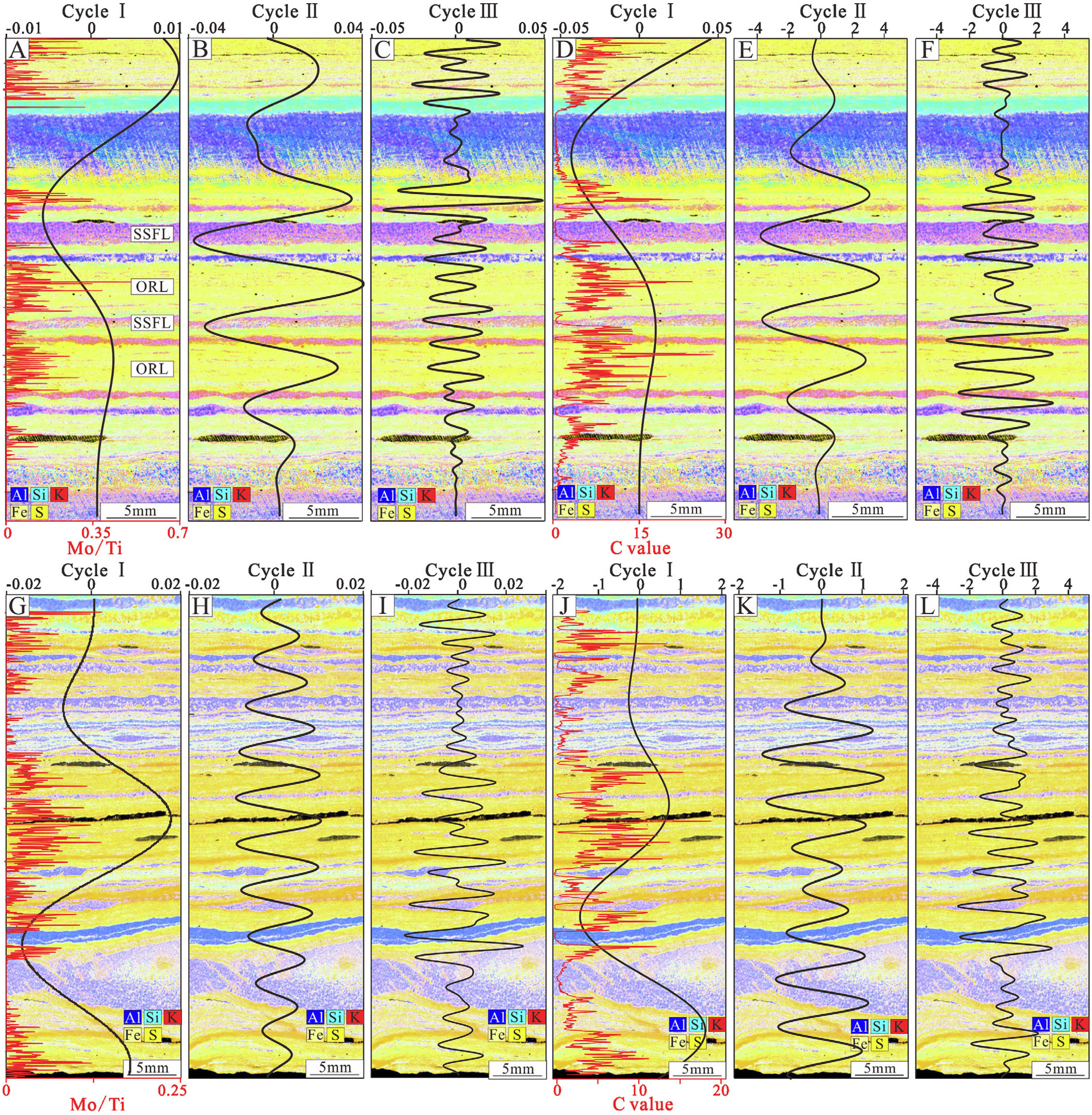

Fig. 7. Filtering results of redox indicator (Mo/Ti) and humidity (C value). Well N70, 1719.20 m, distribution characteristics of Mo/Ti ratio at the micron-scales and filtering results of Mo/Ti ratio on cycle I (Gaussian filter, passband: 0.038 ± 0.011 cycles/mm) (A), cycle II (Gaussian filter, passband: 0.169 ± 0.056 cycles/mm) (B), cycle III (Gaussian filter, passband: 0.546 ± 0.196 cycles/mm) (C). Well N70, 1719.20 m, showing the distribution characteristics of C values at the micron-scales and filtering results of C value on cycle I (Gaussian filter, passband: 0.038 ± 0.011 cycles/mm) (D), cycle II (Gaussian filter, passband: 0.169 ± 0.056 cycles/mm) (E), cycle III (Gaussian filter, passband: 0.546 ± 0.196 cycles/mm) (F). Well N70, 1718.90 m, showing the distribution characteristics of Mo/Ti ratio at the micron-scales and filtering results of Mo/Ti ratio on cycle I (Gaussian filter, passband: 0.041 ± 0.007 cycles/mm) (G), cycle II (Gaussian filter, passband: 0.247 ± 0.016 cycles/mm) (H), cycle III (Gaussian filter, passband: 0.535 ± 0.164 cycles/mm) (I). Well N70, 1718.90 m, showing the distribution characteristics of C values at the micron-scale and filtering results of C value on cycle I (Gaussian filter, passband: 0.041 ± 0.007 cycles/mm) (J), cycle II (Gaussian filter, passband: 0.247 ± 0.016 cycles/mm) (K), cycle III (Gaussian filter, passband: 0.535 ± 0.164 cycles/mm) (L). SSFL – silty-grained felsic lamina; ORL – organic-rich lamina.

et al., 2003; Qiu et al., 2015), which corresponds to an intense period of solar activity in the 360–500 yr cycle I (Fig. 9C–E). During this period, the decreasing Mo/Ti ratios suggest more oxidising conditions, and therefore indicate a period of lake level fall (Brucker et al., 2011) (Fig. 7A, 7G, 9A). The progradation of silty-grained sediments carried by gravity flow mainly occurred towards the center of the lacustrine basin during lake-level drops (Zaragosi et al., 2006; Lericolais et al., 2013; Tombo et al., 2015), thereby depositing SSFL (Fig. 8A, B). The frequency and thickness of SSFL, as well as the grain sizes, gradually increased from proximal to distal palaeo-lake basin (Fig. 4). This further confirms that low-density turbidity currents transported silty-grained sediments

Table 1
Cyclicality of geochemical parameters on thickness and timescales in lacustrine shales from Well N70. Cycle I - III was obtained by spectrum analysis and wavelet analysis. Timescale A indicates the timescale of thickness cycle (cycle I - III) obtained by spectral analysis of Mo/Ti ratio; Timescale B indicates the timescale of thickness cycle (cycle I - III) obtained by spectral analysis of C value.

Well	Depth (m)	Cycle I (mm)	Cycle II (mm)	Cycle III (mm)	Notes
N70	1713.58	22.6614	4.5011	1.6651	Mo/Ti ratio
		22.6614	4.4338	1.6448	C value
N70	1714.08	19.0324	4.6420	1.9032	Mo/Ti ratio
		19.0324	4.6420	1.9032	C value
N70	1714.42	17.9574	5.3472	2.8354	Mo/Ti ratio
		17.9574	5.6175	2.8354	C value
N70	1714.96	22.5527	5.0699	2.6332	Mo/Ti ratio
		22.5527	4.9747	2.6428	C value
N70	1718.30	18.2166	4.2583	2.7099	Mo/Ti ratio
		18.2166	4.2583	2.7324	C value
N70	1718.90	24.2895	4.0483	1.8684	Mo/Ti ratio
		24.2895	4.0483	1.8684	C value
N70	1719.07	26.6810	/	1.4823	Mo/Ti ratio
		26.6810	/	1.5695	C value
N70	1719.20	26.5578	5.9055	1.8327	Mo/Ti ratio
		26.5578	5.9055	1.8669	C value
N70	1720.70	24.4797	5.1926	2.2848	Mo/Ti ratio
		24.4797	5.1926	2.2848	C value
Time scales A		**360–500 yr**	**81–110 yr**	**30–57 yr**	**Mo/Ti ratio**
Time scales B		**360–500 yr**	**81–110 yr**	**30–57 yr**	**C value**

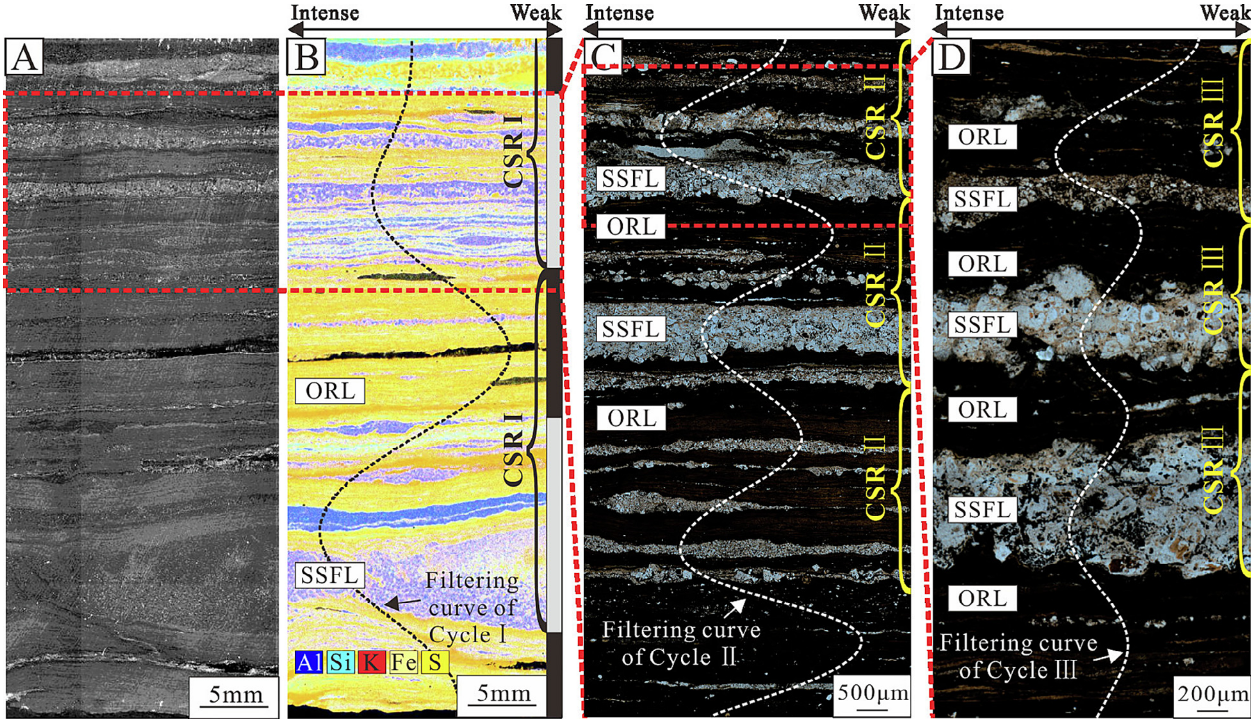

Fig. 8. Cyclical sedimentary records in lacustrine shales and their correspondence to solar activity cycles. (A) Well N70, 1718.90 m, showing the characteristics of bulk shale samples. (B) Centimeter scale sedimentary cycle (CSR I) corresponding to solar activity cycle of 360–500 yr. The filtering curve of Cycle I was obtained by a Gaussian filter (Passband: 0.041 ± 0.007 cycles/mm). Image B was obtained by Micro-XRF scanning of the bulk shale sample in image A. (C) Millimeter scale sedimentary cycle (CSR II) corresponding to solar activity cycle of 81–110 yr. The filtering curve of Cycle II was obtained by a Gaussian filter (Passband: 0.247 ± 0.016 cycles/mm). (D) Millimeter to micron scale sedimentary cycle (CSR III) corresponding to solar activity cycle of 30–57 yr. The filtering curve of Cycle III was obtained by a Gaussian filter (Passband: 0.535 ± 0.164 cycles/mm). Gray rectangle – the strata with several SSFL; black rectangle – ORL; SSFL – silty-grained felsic lamina; ORL – organic-rich lamina.

towards the basin center during lake-level drops (Prins and Postma, 2000; Bourget et al., 2010; Tombo et al., 2015), resulting in several SSFL depositions.

During the weak solar activity period in the 360–500 yr cycle I, δ^{13}C was deficient and the C value was higher, indicating a cold and humid paleoenvironment (Ku and Li, 1998; Paulsen et al., 2003; Qiu et al., 2015). At this stage, lake levels rose and the environment was more reducible, which is indicated by a Mo/Ti ratio that was increasing (Fig. 7A, 7G, and 9A). Only small amounts of thin-bedded SSFL were deposited due to the distal position of the study area with respect to the sediment source, and the limited transportation distances of the sediment gravity flows that transported this material (Tombo et al., 2015). Enhanced rainfall and reducibility during periods of weak solar activity were beneficial for biological prosperity and the preservation of organic matter (Reichwaldt and Ghadouani, 2012). These resulted in enriched clay and organic-

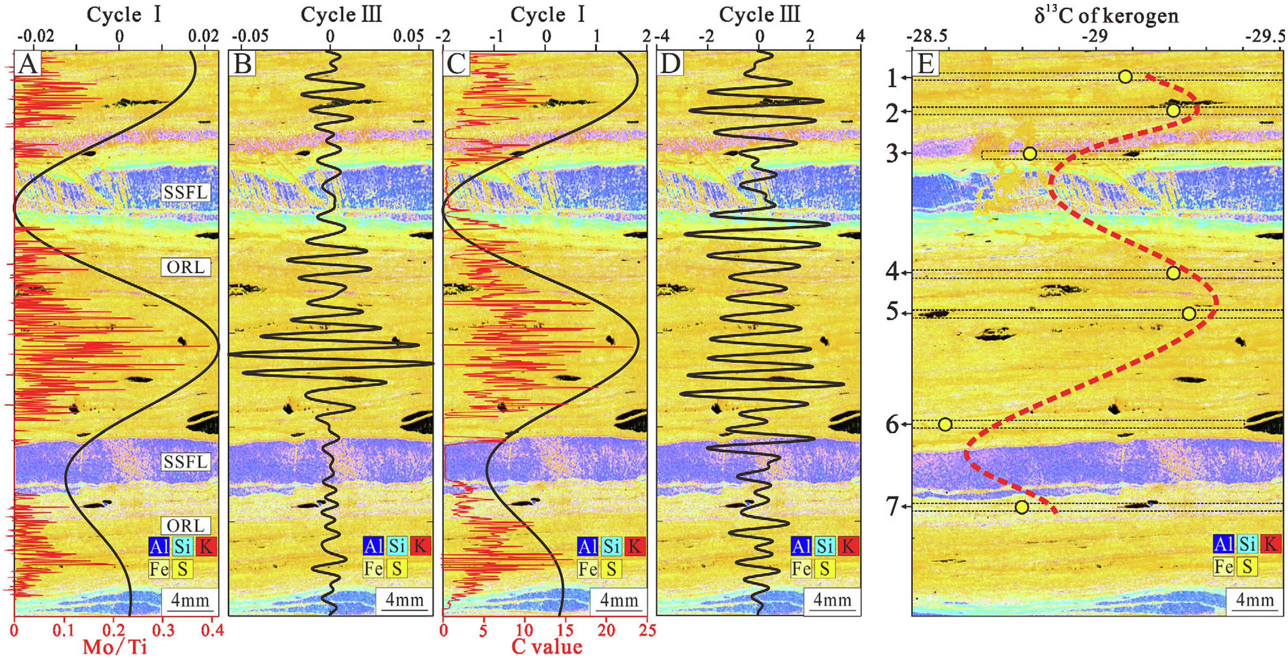

Fig. 9. Filtering results of Mo/Ti ratio and C value and the distribution characteristics of δ^{13}C of kerogen in millimeter-scale in Well N70, 1719.07 m. (A) Distribution characteristics of Mo/Ti ratios and filtering results of Mo/Ti ratios on cycle I (Passband: 0.037 ± 0.003 cycles/mm). (B) Filtering results of Mo/Ti ratios on cycle III (Passband: 0.675 ± 0.162 cycles/mm). (C) Distribution characteristics of C value and filtering results of C value on cycle I (Passband: 0.037 ± 0.003 cycles/mm). (D) Filtering results of C value on cycle III (Passband: 0.637 ± 0.162 cycles/mm). (E) Distribution characteristics of δ^{13}C of kerogen. The black dashed rectangles of 1 to 7 represent the micro-drilling positions. SSFL – silty-grained felsic lamina; ORL – organic-rich lamina.

matter deposition within the clay-rich succession that were deposited during this time (Fig. 8A, B).

The preserved sedimentary record during the intense solar activity period of 360–500 yr cycle I is further complicated by short-term solar activity, as identified as the 81–110 yr (CSR II) and 30–57 yr (CSR III) cycles (Fig. 8A–D). However, these small-scale solar activity cycles are thought to be not strong enough to induce grain-size variations in another semi-cycle of the 360–500 yr cycle I characterized by ORL deposition (Gray et al., 2010; Knudsen et al., 2011) (Fig. 8A–B). The 30–57 yr cycle III matches a lamina couplet (Fig. 8D), indicating that short-term solar activity can induce some short-time lake-level fluctuations under the low-stand background of CSR I. During the weak solar activity period of CSR III, a short-term lake-level rise occurred and interrupted SSFL deposition, forming a small-scale ORL (Fig. 8D). In-situ element scanning shows that the Mo/Ti ratio continually increased during the gradual deposition of the small-scale ORL (Fig. 10A, B), while framboidal pyrite size gradually decreased (Fig. 10A, C), indicating a short-term lake-level rise (Brucker et al., 2011). The δ^{34}S deficit of framboidal pyrite in the ORL compared to the interbedded SSFL further confirms that the paleo-water-depth increased and sedimentation rate decreased in the transition from silt-grade grain deposition to clay-mineral deposition (Richardson et al., 2019; Lang et al., 2021) (Fig. 11).

The solar activity of the 81–110 yr cycle II caused further SSFL thickness variation in different CSR III (Fig. 8C). During the weak solar activity period in the 81–110 yr cycle II, the SSFL was thinner in lamina couplets driven by cycle III, whilst the SSFL became thicker during the intense solar activity period of the 81–110 yr cycle II due to the warm and arid paleoenvironment and lower lake level (Fig. 12A). The grain sizes and thickness of the SSFL also increased during the intense solar activity period of the 81–110 yr cycle II (Fig. 12B–G), further confirming a lower lake level during this period.

5.2. Implications for shale-oil reservoir formation in organic-rich lacustrine shales

Cyclical sedimentary records at the micron to centimeter scales were widespread in the Chang 7_3 sub-member of the Ordos Basin. The high-frequency environmental fluctuation and sedimentary cycles controlled by solar activity (especially 30–57 yr cycle III) provided favorable shale-oil generation and accumulation conditions. During the intense solar activity period in the 360–500 yr cycle I, warm-arid paleoenvironment controlled by 30–57 yr cycle III kept the low lake-level, resulting in the transportation of silty-grained sediments by low-density turbidity currents towards the basin center and SSFL deposition (Figs. 10 and 13A–B). Microscopic observations show that most of the K-feldspars were dissolved to form numerous secondary porosity within the SSFL (Fig. 2B) and these K-feldspar dissolution pores are always observed to be filled with oil (Fig. 14). Therefore, the SSFL deposition in cyclicity shales generally provides a good condition for shale-oil storage. When the paleoenvironment change to cold-humid during the same 30–57 yr cycle III, a short-term lake-level rise occurred, which interrupted SSFL deposition and increased the reducibility of water column (Fig. 10, 13A–B). Meanwhile, a rapid increase in rainfall promoted the input of nutrients into the lake basin in the form of wet deposition and runoff (Reichwaldt and Ghadouani, 2012). Massive inputs of nutrients were beneficial to stimulating biological prosperity and inducing high paleoproductivity (Zhang et al., 2017). In this study, P/Ti ratio was used to analyze the relative level of paleoproductivity (Tribovillard et al., 2006; Wang et al., 2017b). We conducted the spectral analysis of Mo/Ti and P/Ti ratio (Supplementary Data Fig. S4). The results show that the Mo/Ti and P/Ti ratios record the solar activity cycles with similar timescales (Supplementary Data Fig. S4). This indicates that the variation in paleoproductivity in the lake basin is related to solar activity cycle. The increased P/Ti ratios (Fig. 13C) and massive algae blooms (Lin et al.,

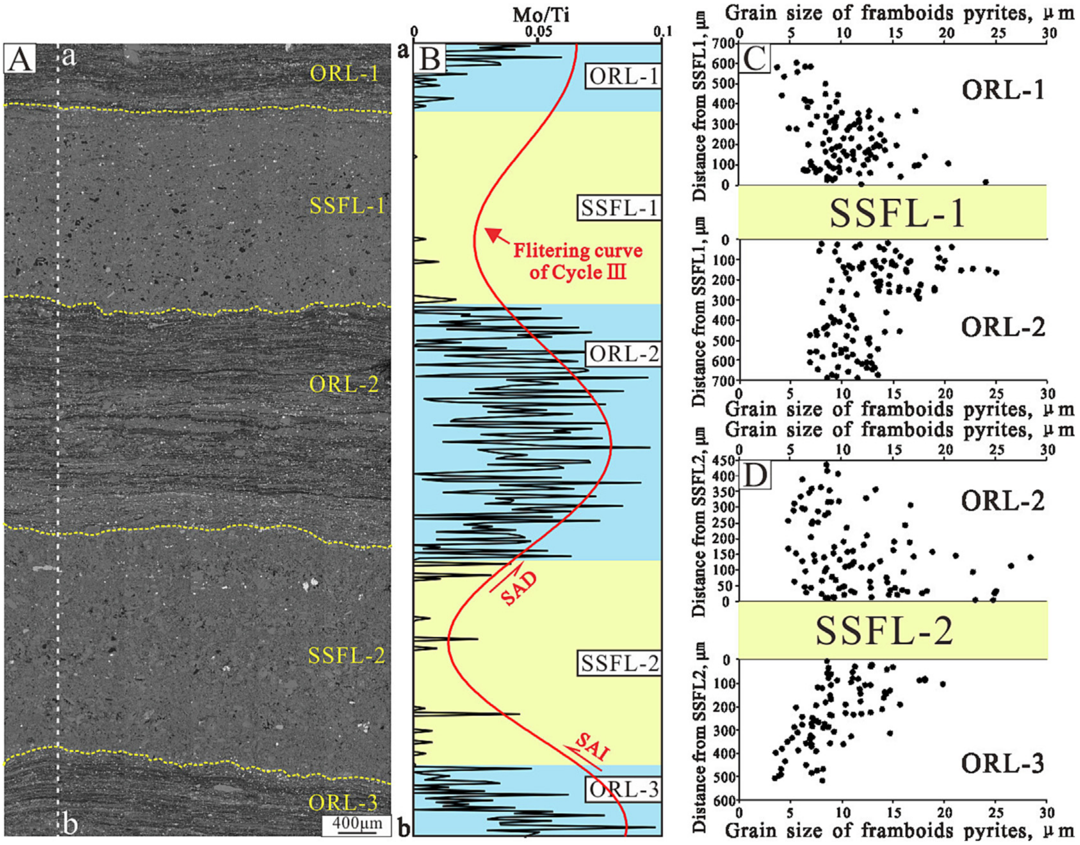

Fig. 10. Microscopic variation of framboidal pyrite sizes and redox indicators in laminar couplets (CSR III). (A) Well N70, 1718.50 m, showing the characteristics of laminar couplets under SEM. (B) Distribution characteristics of Mo/Ti ratios on micron-scale and filtering results of Mo/Ti ratio (cycle III). (C) Variation of framboidal pyrite sizes in ORL-1 and ORL-2 as the distance from SSFL increases. (D) Variation of framboidal pyrite sizes in ORL-2 and ORL-3 as the distance from SSFL increases. SAI – the intensity of solar activity increase; SAD – the intensity of solar activity decrease; SSFL-1, -2 – silty-grained felsic lamina; ORL-1, -2, -3 – organic-rich lamina.

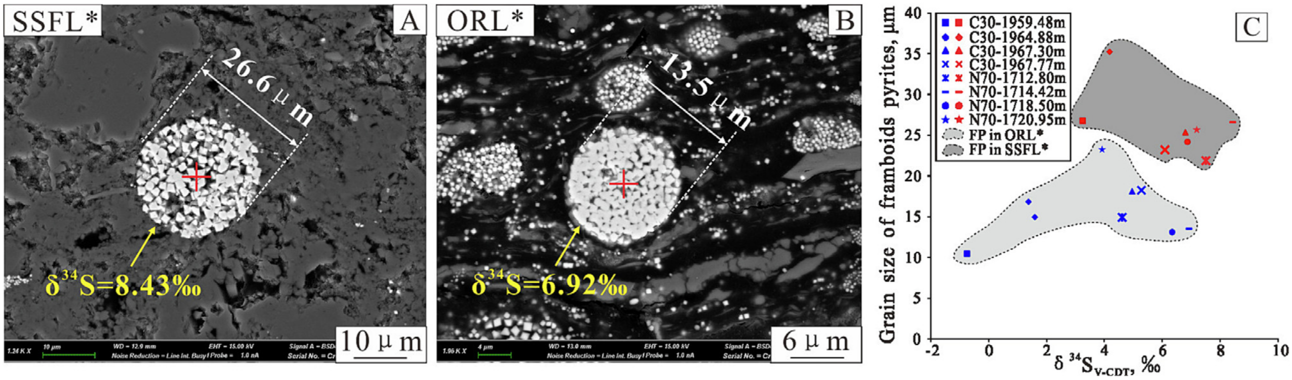

Fig. 11. S isotopic values and grain size of framboidal pyrite in laminar couplets (CSR III). Well N70, 1714.42 m, showing in-situ S isotopic values and grain size of framboidal pyrites in SSFL (A) and ORL (B). (C) In-situ S isotopic values and grain size of framboidal pyrite in SSFL and ORL from different samples. Framboidal pyrites in SSFL generally possess more ^{34}S and have larger diameters than in ORL. The SSFL* and ORL* indicate that the SSFL and ORL are derived from the same pair of laminar couplet. Red cross – the center point of test area in S isotope analysis. (For interpretation of the references to colour in this figure legend, the reader is referred to the web version of this article.)

2023) finally demonstrated that the increase in rainfall induced the improvement of paleoproductivity during the period of weak solar activity in the 30–57 yr cycle III. The co-eval enhancement of paleoproductivity (increased P/Ti ratio) and reducibility (increased Mo/Ti ratio) caused by solar activity favors large amounts of organic matter enrichment in the shale lamina and ORL deposition (Fig. 13A). The TOC content in the ORL reached approximately 20%, which was higher than that in the SSFL (Fig. 13A). The vitrinite reflectance (Ro) of the organic matter in the ORL was distributed from 0.6% to 0.9% (Xi et al., 2020), which is within the oil-generation window, thereby providing high oil-generation potential in ORL. The solar activity of 30–57 yr cycle III induced the steady alternating deposition of ORL and SSFL (Fig. 7). This close "source-reservoir" configuration provides a good foundation for shale-oil reservoir formation.

On this basis, we subsequently conducted a GC–MS analysis of the products extracted from the ORL and SSFL. The mass chromatograms (m/z = 191) exhibit clear similarities (Fig. 13A, D, F, and H). The C_{27}-C_{29} regular steranes in mass chromatograms (m/z = 217) were distributed in a similar "V" shape (Fig. 13A, E, G, I).

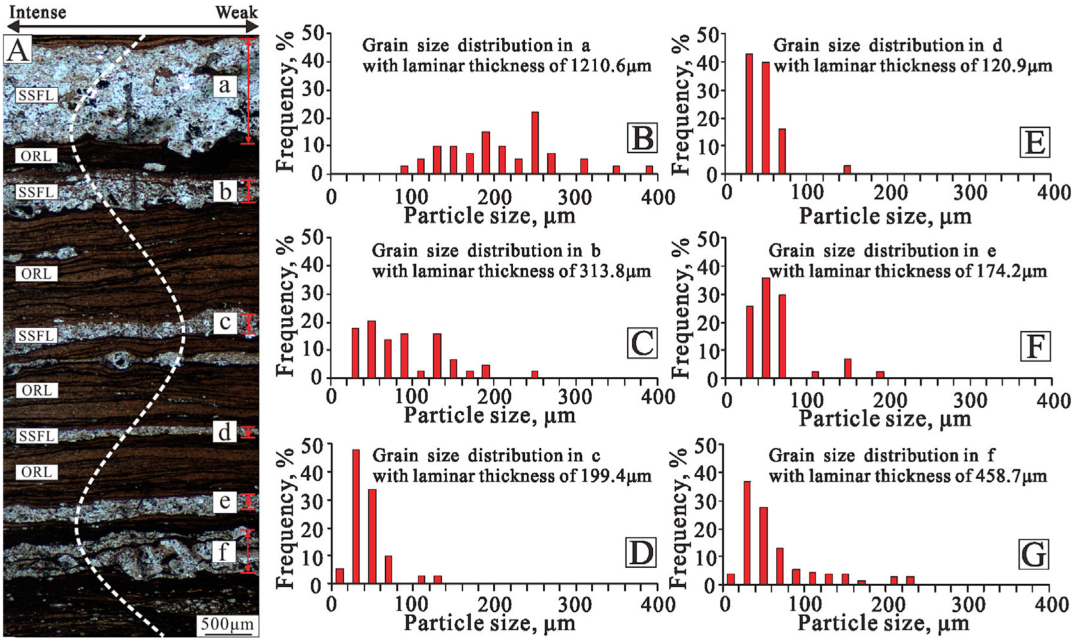

Fig. 12. Relationship between SSFL thickness and grain size of SSFL. (A) SSFL thickness variation in different CSR III. (B–G) Grain-size distribution in lamina a, b, c, d, e, f in image A, respectively. The grains in thicker SSFL always showed coarser grain sizes. SSFL – silty-grained felsic lamina; ORL – organic-rich lamina.

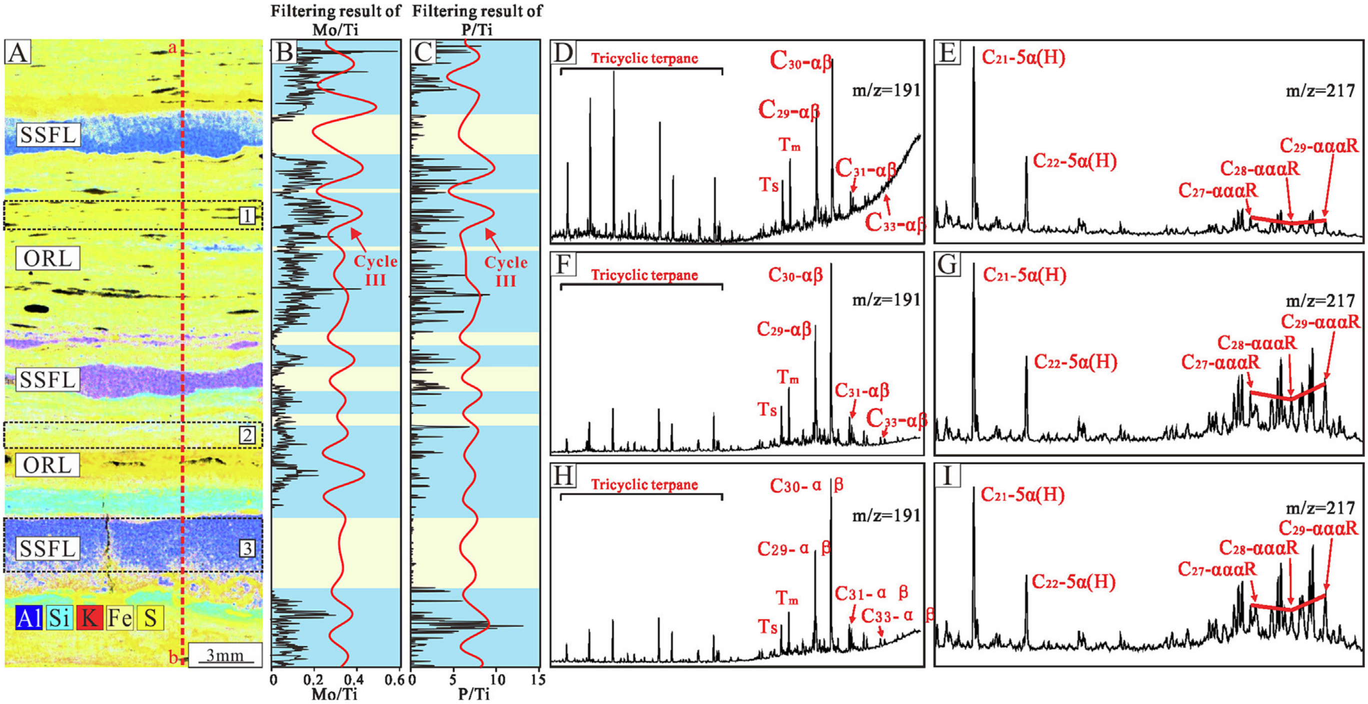

Fig. 13. Paleoproductivity and reducibility evolution recorded in laminated shales and the mass chromatograms of extracted products from ORL and SSFL. (A) Element distribution map after element stacking obtained by Micro-XRF analysis. The black dashed rectangle of 1 to 3 in 'A' represents the micro-drilling positions. TOC content in position 1, 2, and 3 reaches 28.0%, 19.1%, and 10.1%, respectively. (B) Distribution of Mo/Ti ratios from a to b in image 'A' and filtering results of Mo/Ti ratios on cycle III (Gaussian filter, passband: 0.504 ± 0.098 cycles/mm). (C) Distribution of P/Ti ratio from a to b in image 'A' and filtering results of P/Ti ratios on cycle III (Gaussian filter, passband: 0.504 ± 0.098 cycles/mm). (D, F, H) Mass chromatograms (*m*/*z* = 191) of the extracted products from position 1, 2 and 3. (E, G, I) Mass chromatograms (*m*/*z* = 217) of the extracted products from position 1, 2 and 3. Blue rectangle – ORL; yellow rectangle – SSFL; SSFL – silty-grained felsic lamina; ORL – organic-rich lamina. (For interpretation of the references to colour in this figure legend, the reader is referred to the web version of this article.)

These results demonstrate that the oil in the SSFL was sourced from the thermal evolution of organic matter in the adjacent ORL. The same result was obtained using an in situ infrared-spectroscopy analysis (Xi et al., 2020). The excellent case for oil generation and accumulation occurred between ORL and SSFL at the microscale. Therefore, small-scale cyclical sedimentary records provide excellent conditions for oil accumulation in lacustrine shales.

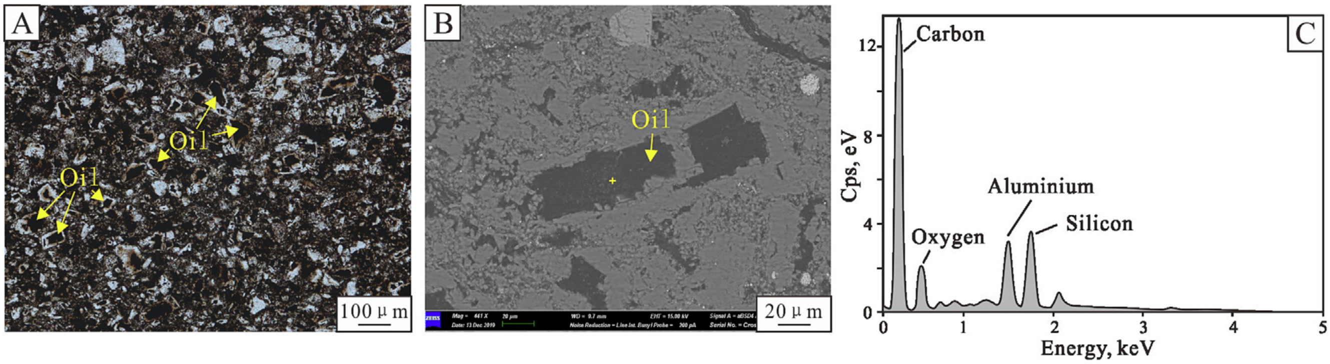

Fig. 14. Characteristics of oil emplacement in feldspar dissolved pores in SSFL. (A) Well C30, 1964.88 m, showing oil charged in feldspar dissolved pores in SSFL, under plane-polarized light. (B) Well C30, 1964.88 m, showing feldspar dissolved pores filled with oil. (C) EDS showing the high energy in the Carbon peak. Yellow cross – the analysis position using EDS. (For interpretation of the references to colour in this figure legend, the reader is referred to the web version of this article.)

6. Conclusions

(1) This study reconstructs high-frequency paleoenvironmental evolution induced by solar activity in the Ordos Basin located in the eastern Tethys during the late Triassic. With the exception of the present study, the influence of solar activity on high-frequency paleoenvironmental evolution in other parts of the globe has not been reported in the Triassic. Whether solar activity had a global effect on paleoenvironmental evolution is yet to be verified in other areas.

(2) Three solar activity cycles (360–500 yr, 81–110 yr, and 30–57 yr) were recorded in lacustrine laminated shales. The cyclic evolution of a warm-arid and cold-humid paleoenvironment caused by solar activity was investigated. The three timescales of the solar activity cycle correspond well with three scales of cyclical sedimentary records (CSR I, II, and III).

(3) High-frequency lake-level fluctuations controlled by solar activity resulted in the formation of cyclical sedimentary records at the micron to centimeter scales. During the intense solar activity period in the 360–500 yr cycle I, a lake-level drop promoted the progradation of silty-grained sediments carried by low-density turbidity currents toward the center of the lacustrine basin, depositing several SSFL. During the period of weak solar activity in the 360–500 yr cycle I, lake-level rise limited occurrence of the gravity flows transporting silty-grained sediments into the lake basin. Coupled with enhanced rainfall and reducibility, ORL was mainly deposited during the period of weak solar activity. Solar activity in the 81–110 yr cycle II and 30–57 yr cycle III further complicated sedimentary records preserved for the intense solar activity period of the 360–500 yr cycle I. In the background of lake-level lowstand, periods of weak solar activity in the 30–57 yr cycle III induced short-term lake-level rise, causing small-scale ORL deposition between the SSFL. The 81–110 yr cycle II caused SSFL thickness variation in different CSR III.

(4) Small-scale cyclical sedimentary records reveal excellent conditions for shale-oil reservoir formation in lacustrine shales. High-frequency paleoenvironmental evolution induced by solar activity, results in the cyclic deposition of SSFL and ORL throughout the thickly-bedded shale interval. Oil produced from ORL directly migrated into the feldspar dissolved pores in the adjacent SSFL, causing large amounts of oil to accumulate within the shale lamina. Therefore, thickly-bedded shales containing large volumes of SSFL may be a favorable target for shale-oil exploration and development.

CRediT authorship contribution statement

Miruo Lin: Conceptualization, Methodology, Investigation, Writing – original draft. **Kelai Xi:** Investigation, Writing – review & editing, Project administration. **Yingchang Cao:** Supervision, Project administration. **Rukai Zhu:** Investigation. **Xiaobing Niu:** Investigation. **Honggang Xin:** Investigation. **Weijiao Ma:** Investigation.

Declaration of Competing Interest

The authors declare that they have no known competing financial interests or personal relationships that could have appeared to influence the work reported in this paper.

Acknowledgement

This study was co-supported by the National Natural Science Foundation of China (Grant No. 42072161), Innovation Research Group of the Natural Fund Committee (Grant No. 41821002) and Fundamental Research Funds for the Central Universities (22CX07008A). We would like to thank the Changqing Oilfield Company of PetroChina for providing the related core samples and geological data in Chang 7_3 sub-member, Ordos Basin. We thank the Editor Prof. Xiaoqiao Wan and Prof. M Santosh for their contributions to the peer review processes of this work, and reviewers for useful comments on earlier versions of this manuscript. We thank Thomas J.H. Dodd for his contribution on the language editing and the constructive comments to ensure that the quality of this work is improved.

Appendix A. Supplementary data

Supplementary data to this article can be found online at https://doi.org/10.1016/j.gsf.2023.101586.

References

Alçiçek, H., Varol, B., Özkul, M., 2007. Sedimentary facies, depositional environments and palaeogeographic evolution of the Neogene Denizli Basin, SW Anatolia Turkey. Sediment. Geol. 202 (4), 596–637.

Anderson, R.Y., Dean, W.E., 1988. Lacustrine varve formation through time. Palaeogeog. Palaeoclimatol. Palaeoecol. 62 (1–4), 215–235.

Anderson, R.Y., Koopmans, L.H., 1963. Harmonic analysis of varve time series. J. Geophys. Res. 68 (3), 877–893.

Andrews, S.D., Trewin, N.H., Hartley, A.J., Weedon, G.P., 2010. Solar variance recorded in lacustrine deposits from the Devonian and Proterozoic of Scotland. J. Geol. Soc London 167, 847–856.

Ayranci, K., Harris, N.B., Dong, T., 2018. Sedimentological and ichnological characterization of the Middle to Upper Devonian Horn River Group, British Columbia, Canada; Insights into mudstone depositional conditions and processes below storm wave-base. J. Sediment. Res. 88 (1), 1–23.

Baas, J.H., Best, J.L., Peakall, J., 2016. Predicting bedforms and primary current stratification in cohesive mixtures of mud and sand. J. Geol. Soc. 173 (1), 12–45.

Baas, J.H., Best, J., Peakall, J., 2021. Rapid gravity flow transformation revealed in a single climbing ripple. Geology 49 (5), 493–497.

Bao, Z.A., Chen, L., Zong, C.L., Yuan, H.L., Chen, K.Y., Dai, M.N., 2017. Development of pressed sulfide powder tablets for in situ sulfur and lead isotope measurement using LA-MC-ICP-MS. Int. J. Mass Spectrom. 421, 255–262.

Berger, A., Loutre, M.F., Dehant, V., 1989. Pre-quaternary Milankovitch frequencies. Nature (London) 342, 6246.

Borrok, D.M., Yang, W., Wei, M., Mokhtari, M., 2019. Heterogeneity of the mineralogy and organic content of the Tuscaloosa Marine Shale. Mar. Pet. Geol. 109, 717–731.

Boulesteix, K., Poyatos-Moré, M., Flint, S.S., Taylor, K.G., Hodgson, D.M., Hasiotis, S.T., 2019. Transport and deposition of mud in deep-water environments: Processes and stratigraphic implications. Sedimentology 66 (7), 2894–2925.

Bourget, J., Zaragosi, S., Ellouz-Zimmermann, S., Ducassou, E., Prins, M.A., Garlan, T., Lanfumey, V., Schneider, J.L., Rouillard, P., Giraudeau, J., 2010. Highstand vs. lowstand turbidite system growth in the Makran active margin: Imprints of high-frequency external controls on sediment delivery mechanisms to deep water systems. Mar. Geol. 274, 187–208.

Brucker, R.P., McManus, J., Severmann, S., Owens, J., Lyons, T.W., 2011. Trace metal enrichments in Lake Tanganyika sediments: Controls on trace metal burial in lacustrine systems. Geochim. Cosmochim. Acta 75 (2), 483–499.

Carroll, A.R., Graham, S.A., Smith, M.E., 2010. Walled sedimentary basins of China. Basin Res. 22 (1), 17–32.

Carslaw, K.S., Harrison, R.G., Kirkby, J., 2002. Cosmic rays, clouds, and climate. Science 198 (5599), 1732–1737.

Chen, L., Chen, K.Y., Bao, Z.A., Liang, P., Sun, T.T., Yuan, H.L., 2017. Preparation of standards for in situ sulfur isotope measurement in sulfide using femtosecond laser ablation MC-ICP-MS. JAAS 32, 107–116.

Chu, G., Liu, J., Schettler, G., Li, J., Sun, Q., Gu, Z., Lu, H., Liu, Q., Liu, T., 2005. Sediment fluxes and varve formation in Sihailongwan, a maar lake from northeastern China. J. Paleolimnol. 34 (3), 311–324.

Clausing, A., Boy, J.A., 2000. Lamination and primary production in fossil lakes: relationship to paleoclimate in the Carboniferous- Permian transition. Geol. Soc. London Spec. Pub. 181 (1), 5–16.

Cooper, M.C., O'Sullivana, P.E., Shineb, A.J., 2000. Climate and solar variability recorded in Holocene laminated sediments-a preliminary assessment. Quat. Int. 68–71, 363–371.

Corso, D.J., Ruffell, A., Preto, N., 2018. The Carnian pluvial episode (Late Triassic): new insights into this important time of global environmental and biological change. J. Geol. Soc. 175 (6), 986–988.

Dal Corso, J., Bernardi, M., Sun, Y., Song, H., Seyfullah, L.J., Preto, N., Gianolla, P., Ruffell, A., Kustatscher, E., Roghi, G., Merico, A., Hohn, S., Shmidt, A.R., Marzoli, A., Newton, R., Wignall, P.B., Benton, M.J., 2020. Extinction and dawn of the modern world in the Carnian (Late Triassic). Sci. Adv. 6, eaba0099.

Damon, P.E., Sonnett, C.P., 1991. Solar and terrestrial components of the atmospheric ^{14}C variation spectrum. In: Sonnett, C.P., Giampapa, M.S., Matthews, M.S. (Eds.), The Sun in Time. The University of Arizona Press, Tucson, Ariz., pp. 360–388.

Dicke, R.H., 1979. Solar luminosity and the sunspot cycle. Nature 280 (5717), 24–27.

Ernesto, M., Pacca, I.G., 1981. Spectral analysis of Permocarboniferous geomagnetic variation data from glacial rhythmites. Geophys. J. Int. 67, 641–647.

Fu, J.H., Li, S.X., Xu, L.M., Niu, X.B., 2018. Paleo-sedimentary environmental restoration and its significance of Chang 7 Member of Triassic Yanchang Formation in Ordos Basin NW China. Petroleum Explor. Dev. 45 (6), 998–1008.

Fu, J.H., Niu, X.B., Dan, W.D., Feng, S.B., Liang, X.W., Xin, H.G., You, Y., 2019. The geological characteristics and the progress on exploration and development of shale oil in Chang7 Member of Mesozoic Yanchang Formation Ordos Basin. China Petroleum Explor. 24 (5), 601–614.

Fu, J.H., Li, S.X., Niu, X.B., Deng, X.Q., Zhou, X.P., 2020. Geological characteristics and exploration of shale oil in Chang 7 Member of Triassic Yanchang Formation, Ordos Basin NW China. Petroleum Explor. Dev. 47 (5), 931–945.

Gabbott, S.E., Zalasiewicz, J., Aldridge, R.J., Theron, J.N., 2010. Eolian input into the Late Ordovician postglacial Soom Shale South Africa. Geology 38 (12), 1103–1106.

Galloway, J.M., Wigstion, A., Patterson, R.T., Swindles, G.T., Reinhardt, E., Roe, H.M., 2013. Climate change and decadal to centennial-scale periodicities recorded in a late Holocene NE Pacific marine record: Examining the role of solar forcing. Palaeogeog. Palaeoclimatol. Palaeoecol. 386, 669–689.

Gray, L.J., Beer, J., Geller, M., Haigh, J.D., Lockwood, M., Matthes, K., Cubasch, U., Fleitmann, D., Harrison, G., Hood, L., Luterbacher, J., Meehl, G.A., Shindell, D., van Geel, B., White, W., 2010. Solar influences on climate. Rev. Geophys. 48, RG4001.

Hammer, Ø., Harper, D.A., Ryan, P.D., 2001. PAST: Paleontological statistics software package for education and data analysis. Palaeontol. Electron. 4 (1), 9.

Heydari, E., Wade, W.J., Anderson, L.C., 1997. Depositional environments, organic carbon accumulation, and solar-forcing cyclicity in Smackover Formation lime mudstones, northern Gulf Coast. AAPG Bull. 81, 760–774.

Hinnov, L.A., 2000. New perspectives on orbitally forced stratigraphy. Annu. Rev. Earth Planet. Sci. 28 (1), 419–475.

Hornung, T., Krystyn, L., Brandner, R., 2007. A Tethys-wide mid-Carnian (Upper Triassic) carbonate productivity crisis: evidence for the Alpine Reingraben event from Spiti (Indian Himalaya)? J. Asian Earth Sci. 30 (2), 285–302.

Hoyt, D.V., Schatten, K.H., 1998. Group sunspot numbers: a new solar activity reconstruction. Sol. Phys. 179, 189–219.

Huang, C., Zhang, J., Hua, W., Yue, J., Lu, Y., 2018. Sedimentology and lithofacies of lacustrine shale: A case study from the Dongpu sag, Bohai Bay Basin, Eastern China. J. Nat. Gas Sci. Eng. 60, 174–189.

Hughen, K.A., Overpeck, J.T., Peterson, L.C., Anderson, R.F., 1996. The nature of varved sedimentation in the Cariaco Basin, Venezuela, and its palaeoclimatic significance. Geol. Soc. London Spec. Pub. 116 (1), 171–183.

Hughes, G.B., Giegengack, R., Kritikos, H.N., 2003. Modern spectral climate patterns in rhythmically deposited argillites of the Gowganda Formation (Early Proterozoic), southern Ontario Canada. Earth Planet. Sci. Lett. 207, 13–22.

Ilyashuk, B., Gobet, E., Heiri, O., Lotter, A.F., van Leeuwen, J.F.N., van der Knaap, W.O., Ilyashuk, E., Oberli, F., Ammann, B., 2009. Lateglacial environmental and climatic changes at the Maloja Pass, Central Swiss Alps, as recorded by chironomids and pollen. Quat. Sci. Rev. 18, 1340–1353.

Jarvie, D.M., 2012. Shale resource systems for oil and gas: Part 2-Shale-oil resource systems. In: Breyer, J.A. (Ed.), Shale Reservoirs-Giant Resources for the 21st Century, vol. 97. AAPG Memoir, 89-119.

Jin, Z.J., Zhu, R.K., Liang, X.P., Shen, Y.Q., 2021. Several issues worthy of attention in current lacustrine shale oil exploration and development. Petroleum Explor. Dev. 48 (6), 1–12.

Kiessling, W., 2010. Reef expansion during the Triassic: Spread of photosymbiosis balancing climatic cooling. Palaeogeog. Palaeoclimatol. Palaeoecol. 290 (1–4), 11–19.

Kilian, L., 2016. The impact of the shale oil revolution on US oil and gasoline prices. Rev. Environ. Econ. Policy 10 (2), 185–205.

Kniveton, D.R., Todd, M.C., 2001. On the relationship of cosmic ray flux and precipitation. Geophys. Res. Lett. 28 (8), 1527–1530.

Knudsen, M.F., Jacobsen, B.H., Riisager, P., Olsen, J., Seidenkrantz, M., 2011. Evidence of Suess solar-cycle bursts in subtropical Holocene speleothem δ^{18}O records. Holocene 22 (5), 597–602.

Könitzer, S.F., Davies, S.J., Stephenson, M.H., Leng, M.J., 2014. Depositional controls on mudstone lithofacies in a basinal setting: implications for the delivery of sedimentary organic matter. J. Sediment. Res. 84 (3), 198–214.

Ku, T.L., Li, C.H., 1998. Speleothems as high-resolution paleoenvironment archives: records from northeastern China. Proceedings of the Indian Academy of Sciences-Earth and Planetary Sciences 107, 321–330.

Kuehn, H., Lembke-Jene, L., Gersonde, R., Esper, O., Lamy, F., Arz, H., Kuhn, G., Tiedemann, R., 2014. Laminated sediments in the Bering Sea reveal atmospheric teleconnections to Greenland climate on millennial to decadal timescales during the last deglaciation. Clim. Past 10, 2215–2236.

Lang, X.G., Zhao, Z.Q., Ma, H.R., Huang, K.J., Li, S.Z., Zhou, C.M., Xiao, S.H., Peng, Y.B., Liu, Y.G., Tang, W.B., Shen, B., 2021. Cracking the superheavy pyrite enigma: possible roles of volatile organosulfur compound emission. Nat. Sci. Rev. nwab034.

Lericolais, G., Bourget, J., Popescu, I., Jermannaud, P., Mulder, T., Jorry, S., Panin, N., 2013. Late Quaternary deep-sea sedimentation in the western Black Sea: new insights from recent coring and seismic data in the deep basin. Global Planet. Change 103, 232–247.

Li, M., Kump, L.R., Hinnov, L.A., Mann, M.E., 2018b. Tracking variable sedimentation rates and astronomical forcing in Phanerozoic paleoclimate proxy series with evolutionary correlation coefficients and hypothesis testing. Earth Planet. Sci. Lett. 501, 165–179.

Li, K.J., Su, T.W., Liang, H.F., 2004. Cycle of sunspot activity based on modern observation. Chinese Sci. Bull. 49, 2511–2516.

Li, P., Tang, D., Shi, X., Jiang, G., Zhao, X., Zhou, X., Wang, X., Chen, X., 2018a. Sunspot cycles recorded in siliciclastic biolaminites at the dawn of the Neoproterozoic Sturtian glaciation in South China. Precambrian Res. 315, 75–91.

Liang, C., Cao, Y.C., Liu, K.Y., Jiang, Z.X., Wu, J., Hao, F., 2018. Diagenetic variation at the lamina scale in lacustrine organic-rich shales: implications for hydrocarbon migration and accumulation. Geochim. Cosmochim. Acta 229, 112–128.

Lin, M., Xi, K., Cao, Y., Liu, K., Zhu, R., 2023. Periodic paleo-environment oscillation on multi-timescales in the Triassic and their significant implications for algal blooms: A case study on the lacustrine shales in Ordos Basin. Palaeogeog. Palaeoclimatol. Palaeoecol. 612, 111376.

Liu, X.Y., Li, S.X., Guo, Q.H., Zhou, X.P., Liu, J.Y., 2021. Characteristics of rock types and exploration significance of the shale strata in the Chang 7_3 submember of Yanchang Formation Ordos Basin. Natural Gas Geoscience 32 (8), 1177–1189.

Liu, X.K., Rao, Z.G., Shen, C.C., Liu, J.B., Chen, J.H., Chen, S.Q., Wang, X.F., Chen, F.H., 2019. Holocene solar activity imprint on centennial- to multidecadal- scale hydroclimatic oscillations in arid Central Asia. J. Geophys. Res. Atmos. 124 (5), 2562–2573.

Lu, J., Zhang, P., Dal Corso, J., Yang, M., Wignall, P. B., Greene, S. E., Shao, L. Y., Lyu, D., Hilton, J., 2021. Volcanically driven lacustrine ecosystem changes during the Carnian Pluvial Episode (Late Triassic). Proc. Nat. Acad. Sci. 118(40), e2109895118.

Lucio, P.S., 2005. Learning with solar activity influence on Portugal's rainfall: a stochastic overview. Geophys. Res. Lett. 32, L23819.

Lückge, A., Doose-Rolinski, H., Khan, A.A., Schulz, H., Rad, U.V., 2001. Monsoonal variability in the northeastern Arabian Sea during the past 5000 years: geochemical evidence from laminated sediments. Palaeogeog. Palaeoclimatol. Palaeoecol. 167 (3–4), 273–286.

Ma, C., Hinnov, L.A., Eldrett, J.S., Meyers, S.R., Bergman, S.C., Minisini, D., Lutz, B., 2022. Centennial to millennial variability of greenhouse climate across the mid-Cenomanian event. Geology 50 (2), 227–231.

Magny, M., Arnaud, F., Holzhauser, H., Chapron, E., Debret, M., Desmet, M., Leroux, A., Millet, L., Revel, M., Vannière, B., 2010. Solar and proxy-sensitivity imprints on paleohydrological records for the last millennium in west-central Europe. Quat. Res. 73, 173–179.

Makeen, Y.M., Abdullah, W.H., Ayinla, H.A., Shan, X.L., Liang, Y., Su, S.Y., Noor, N.M., Hasnan, H.K., Asiwaju, L., 2019. Organic geochemical characteristics and depositional setting of Paleogene oil shale, mudstone and sandstone from onshore Penyu Basin, Chenor, Pahang Malaysia. Int. J. Coal Geol. 207, 52–72.

Mănescu, C.B., Nuno, G., 2015. Quantitative effects of the shale oil revolution. Energy Policy 86, 855–866.

Mao, X.M., Cheng, S.G., Hong, Y.T., Zhu, Y.X., Wang, F.L., 2009. The influence of volcanism on paleoclimate in the northeast of China: Insights from Jinchuan peat, Jilin Province China. Chin. J. Geochem. 28, 212–219.

Martínek, K., Blecha, M., Daněk, V., Francu, J., Hladíková, J., Johnová, R., Uličný, D., 2006. Record of palaeoenvironmental changes in a Lower Permian organic-rich lacustrine succession: integrated sedimentological and geochemical study of the Rudník member, Krkonoše Piedmont Basin Czech Republic. Palaeogeog. Palaeoclimatol. Palaeoecol. 230 (1–2), 85–128.

Martín-Puertas, C., Valero-Garcés, B.L., Mata, M.P., Moreno, A., Giralt, S., Martínez-Ruiz, F., Jiménez-Espejo, F., 2011. Geochemical processes in a Mediterranean Lake: a high-resolution study of the last 4,000 years in Zonar Lake, southern Spain. J. Paleolimnol. 46 (3), 405–421.

Milana, J.P., Lopez, S., 1998. Solar cycles recorded in Carboniferous glacimarine rhythmites (Western Argentina): relationships between climate and sedimentary environment. Palaeogeog. Palaeoclimatol. Palaeoecol. 144, 37-63.
Moreno, A., 2012. A Multiproxy Paleoclimate Reconstruction over the Last 250 kyr from Marine Sediments: The Northwest African Margin and the Western Mediterranean Sea. In: Hublin, J.J., McPherron, S. (Eds), Modern Origins. Vertebrate Paleobiology and Paleoanthropology. Springer, Dordrecht. https://doi.org/10.1007/978-94-007-2929-2_1.

Natalicchio, M., Pierre, F.D., Birgel, D., Brumsack, H., Carnevale, G., Gennari, R., Gier, R., Lozar, F., Pellegrino, L., Sabino, M., Schnetger, B., Peckmann, J., 2019. Paleoenvironmental change in a precession-paced succession across the onset of the Messinian salinity crisis: Insight from element geochemistry and molecular fossils. Palaeogeog. Palaeoclimatol. Palaeoecol. 518, 45–61.

Olsen, P.E., Kent, D.V., 1996. Milankovitch climate forcing in the tropics of Pangaea during the Late Triassic. Palaeogeog. Palaeoclimatol. Palaeoecol. 122, 1–26.

Park, J., 2017. Solar and tropical ocean forcing of late-Holocene climate change in coastal East Asia. Palaeogeog. Palaeoclimatol. Palaeoecol. 469, 74–83.

Park, M.H., Fürsich, F., 2001. Cyclic nature of lamination in the Tithonian Solnhofen Plattenkalk of southern Germany and its palaeoclimatic implications. Int. J. Earth Sci. 90, 847–854.

Paulsen, D.E., Li, H.C., Ku, T.L., 2003. Climate variability in central China over the last 1270 years revealed by high-resolution stalagmite records. Quat. Sci. Rev. 22 (5–7), 691–701.

Peng, J.W., 2020. Sedimentology of the Upper Pennsylvanian organic-rich Cline Shale, Midland Basin: From gravity flows to pelagic suspension fallout. Sedimentology 68 (2), 805–833.

Percival, L.M., Ruhl, M., Hesselbo, S.P., Jenkyns, H.C., Whiteside, J.H., 2017. Mercury evidence for pulsed volcanism during the end-Triassic mass extinction. Proc. Nat. Acad. Sci. 114 (30), 7929–7934.

Pollastro, R.M., 2007. Total petroleum system assessment of undiscovered resources in the giant Barnett Shale continuous (unconventional) gas accumulation, Fort Worth Basin Texas. AAPG Bulletin 91 (4), 551–578.

Preto, N., Kustatscher, E., Wignall, P.B., 2010. Triassic climates-state of the art and perspectives. Palaeogeog. Palaeoclimatol. Palaeoecol. 290 (1–4), 1–10.

Prins, M.A., Postma, G., 2000. Effects of climate, sea level, and tectonics unraveled for last deglaciation turbidite records of the Arabian Sea. Geology 28 (4), 375–378.

Qiu, X.W., Liu, C.Y., Mao, G.Z., Deng, Y., Wang, F.F., Wang, J.Q., 2015. Major, trace and platinum-group element geochemistry of the Upper Triassic nonmarine hot shales in the Ordos basin, Central China. Appl. Geochem. 53, 42–52.

Reichwaldt, E.S., Ghadouani, A., 2012. Effects of rainfall patterns on toxic cyanobacterial blooms Bin a changing climate: Between simplistic scenarios and complex dynamics. Water Res. 46 (5), 1372–1393.

Reid, G.C., 2000. Solar Variability and the earth's climate: introduction and overview. Space Sci. Rev. 94, 1–11.

Richardson, J.A., Keating, C., Lepland, A., Hints, O., Fike, D.A., 2019. Silurian records of carbon and sulfur cycling from Estonia: The importance of depositional environment on isotopic trends. Earth Planet. Sci. Lett. 512, 71–82.

Ripepe, M., Roberts, L.T., Fischer, A.G.B., 1991. ENSO and sunspot cycles in varved Eocene oil shales from image analysis. J. Sediment. Res. 61 (7), 1155–1163.

Saif, T., Lin, Q., Butcher, A.R., Bijeljic, B., Blunt, M.J., 2017. Multi-scale multi-dimensional microstructure imaging of oil shale pyrolysis using X-Ray micro-tomography, automated ultra-high resolution SEM. MAPS Mineralogy and FIB-SEM. Applied Energy 202 (15), 628–647.

Schaaf, M., Thurow, J., 1998. Two 30,000 year high-resolution greyvalue time series from the Santa Barbara Basin and the Guaymas Basin. Geol. Soc. London Spec. Pub. 131 (1), 101–110.

Schieber, J., Southard, J.B., Schimmelmann, A., 2010. Lenticular shale fabrics resulting from intermittent erosion of water-rich muds-interpreting the rock record in the light of recent flume experiments. J. Sediment. Res. 80 (1), 119–128.

Schulz, M., Mudelsee, M., 2002. REDFIT: estimating red-noise spectra directly from unevenly spaced paleoclimatic time series. Comput. Geosci. 28, 421–426.

Scotese, C.R., 2014. Atlas of Permo-Carboniferous Paleogeographic Maps (Mollweide Projection), Maps 53–64, Volumes 4. The Late Paleozoic, PALEOMAP Atlas for ArcGIS, PALEOMAP Project, Evanston, IL.

Shi, J.Y., Jin, Z.J., Liu, Q.Y., Fan, T.L., Gao, Z.Q., 2021. Sunspot cycles recorded in Eocene lacustrine fine-grained sedimentary rocks in the Bohai Bay Basin, eastern China. Global Planet. Change 205, 103614.

Shunk, A.J., Driese, S.G., Dunbar, J.A., 2009. Late Tertiary paleoclimatic interpretation from lacustrine rhythmites in the Gray Fossil Site, northeastern Tennessee, USA. J. Paleolimnol. 42, 11–24.

Solanki, S.K., Usoskin, I.G., Kromer, B., Schüssler, M., Beer, J., 2004. Unusual activity of the Sun during recent decades compared to the previous 11,000 years. Nature 431 (7012), 1084–1087.

Song, M.S., Liu, H.M., Wang, Y., Liu, Y.L., 2020. Enrichment rules and exploration practices of Paleogene shale oil in Jiyang Depression, Bohai Bay Basin China. Petroleum Explor. Dev. 47 (2), 242–253.

Song, M., Zhou, A., Zhang, X., Zhao, C., He, Y., Yang, W., Liu, W., Li, S., Liu, Z., 2015. Solar imprints on Asian inland moisture fluctuations over the last millennium. Holocene 25 (12), 1935–1943.

Speight, J.G., 2012. Shale Oil Production Processes. Gulf Professional Publishing, 1st ed. Elsevier.

Stanley, D.J., 1983. Parallel laminated deep-sea muds and coupled gravity flow-hemipelagic settling in the Mediterranean. Smithson. Contrib. Mar. Sci. 19, 1–17.

Steenbrink, J., Kloosterboer-van Hoeve, M.L., Hilgen, F.J., 2003. Millennial-scale climate variations recorded in Early Pliocene colour reflectance time series from the lacustrine Ptolemais Basin (NW Greece). Global Planet. Change 36 (1–2), 47–75.

Stow, D.A., Shanmugam, G., 1980. Sequence of structures in fine-grained turbidites: comparison of recent deep-sea and ancient flysch sediments. Sediment. Geol. 25 (1–2), 23–42.

Sun, Y.D., Wignall, P.B., Joachimski, M.M., Bond, D.P., Grasby, S.E., Lai, X.L., Wang, L. N., Zhang, Z.T., Sun, S., 2016. Climate warming, euxinia and carbon isotope perturbations during the Carnian (Triassic) Crisis in South China. Earth Planet. Sci. Lett. 444, 88–100.

Tänavsuu-Milkeviciene, K., Frederick Sarg, J., 2012. Evolution of an organic-rich lake basin-stratigraphy, climate and tectonics: Piceance Creek basin. Eocene Green River Formation. Sedimentology 59 (6), 1735–1768.

Tian, X., Gao, Y., Kukla, T., Lenz, O., Huang, H., Ibarra, D.E., Sun, S.L., Wang, C.S., 2021. Early Cretaceous solar cycles recorded in lacustrine laminations in North China. Am. J. Sci. 321 (9), 1285–1307.

Tombo, S.L., Dennielou, B., Berne, S., Bassetti, M.A., Toucanne, S., Jorry, S.J., Jouet, G., Fontanier, C., 2015. Sea-level control on turbidite activity in the Rhone canyon and the upper fan during the Last Glacial Maximum and Early deglacial. Sediment. Geol. 323, 148–166.

Tribovillard, N., Algeo, T.J., Lyons, T., Riboulleau, A., 2006. Trace metals as paleoredox and paleoproductivity proxies: an update. Chem. Geol. 232 (1–2), 12–32.

Valero, L., Garcés, M., Cabrera, L., Costa, E., Sáez, A., 2014. 20 Myr of eccentricity paced lacustrine cycles in the Cenozoic Ebro Basin. Earth Planet. Sci. Lett. 408 (15), 183–193.

van Geel, B., Raspopov, O.M., Renssen, H., Plicht, V.D., Dergachev, V.A., Meijer, H.A.J., 1999. The role of solar forcing upon climate change. Quat. Sci. Rev. 18, 331–338.

Vonrad, U., Khan, A.A., Berger, W.H., Rammlmair, D., Treppke, U., 2002. Varves, turbidites and cycles in upper Holocene sediments (Makran slope, northern Arabian Sea). Geol. Soc. London Spec. Pub. 195 (1), 387–406.

Walters, A.P., Meyers, S.R., Carroll, A.R., Hill, T.R., Vanden Berg, M.D., 2020. Lacustrine cyclicity in the early Eocene Green River Formation, Uinta Basin, Utah: Evidence from X-ray fluorescence core scanning. J. Sediment. Res. 90 (4), 429–447.

Wang, Y.J., Cheng, H., Edwards, R.L., He, Y.Q., Kong, X.G., An, Z.S., Wu, J.Y., Kelly, M.J., Dykoski, C.A., Li, X.D., 2005. The Holocene Asian monsoon: links to solar changes and North Atlantic climate. Science 308 (5723), 854–856.

Wang, R.G., Li, W.H., Liao, Y.Y., Guo, Y.Q., Liu, H.W., 2013. Provenance analysis of Chang 7 Member of Triassic Yanchang Formation in Ordos Basin. Geol. Bull. China 32 (4), 671–684.

Wang, J.Q., Liu, C.Y., Li, H., Wu, T.T., Wu, J.L., 2017a. Geochronology, potential source and regional implication of tuff intervals in Chang 7 member of Yanchang Formation, south of Ordos basin. Acta Sediment. Sin. 35 (4), 691–704.

Wang, C., Wang, Q., Chen, G., He, L., Xu, Y., Chen, L., Chen, D., 2017b. Petrographic and geochemical characteristics of the lacustrine black shales from the Upper Triassic Yanchang Formation of the Ordos Basin, China: implications for the organic matter accumulation. Mar. Pet. Geol. 86, 52–65.

Washburn, K.E., Birdwell, J.E., Foster, M., Gutierrez, F., 2015. Detailed description of oil shale organic and mineralogical heterogeneity via Fourier transform infrared microscopy. Energy Fuels 29 (7), 4264–4271.

Wilhelms, A., Larter, S.R., Leythaeuser, D., Dypvik, H., 1989. Recognition and quantification of the effects of primary migration in a Jurassic clastic source-rock from the Norwegian continental shelf. Adv. Org. Geochem. 16 (1–3), 103–113.

Xi, K.L., Li, K., Cao, Y.C., Lin, M.R., Niu, X.B., Zhu, R.K., Wei, X.Z., You, Y., Liang, X.W., Feng, S.B., 2020. Laminae combination and shale oil enrichment patterns of Chang 7_3 sub-member organic-rich shales in the Triassic Yanchang Formation, Ordos Basin NW China. Petroleum Explor. Dev. 47 (6), 1342–1353.

Xu, K., Chen, H.H., Huang, C.J., Ogg, J.G., Zhu, J.X., Lin, S.Q., Yang, D.Q., Zhao, P., Kong, L.T., 2019. Astronomical time scale of the Paleogene lacustrine paleoclimate record from the Nanxiang Basin, central China. Palaeogeog. Palaeoclimatol. Palaeoecol. 532, 109253.

Yang, H., Dou, W.T., Liu, X.Y., Zhang, C.L., 2010. Analysis on sedimentary facies of member 7 in Yanchang Formation of Triassic in Ordos Basin. Acta Sedmentologica Sinica 28 (2), 254–263.

Yang, M.H., Liu, C.Y., Zheng, M.L., Lan, C.L., Tang, X., 2007. Sequence framework of two different kinds of margins and their response to tectonic activity during the Middle-Late Triassic, Ordos Basin. Sci. China Ser. D Earth Sci. 50, 203–216.

Yin, Z.Q., Ma, L.H., Han, Y.B., Han, Y.G., 2007. Long-term variations of solar activity. Chinese Sci. Bull. 52 (20), 2737–2741.

Zaragosi, S., Bourillet, J.F., Eynaud, F., Toucanne, S., Denhard, B., Toer, A.V., Lanfumey, V., 2006. The impact of the last European deglaciation on the deep-sea turbidite systems of the Celtic-Armorican margin (Bay of Biscay). Geo-Mar. Lett. 26, 317–329.

Zhang, K., Liu, R., Liu, Z.J., Li, B.L., Han, J.B., Zhao, K.G., 2020. Influence of volcanic and hydrothermal activity on organic matter enrichment in the Upper Triassic Yanchang Formation, southern Ordos Basin,. Central China. Mar. Pet. Geol. 112, 104059.

Zhang, W.Z., Yang, H., Xia, X.Y., Xie, L.Q., Xie, G.W., 2016. Triassic chrysophyte cyst fossils discovered in the Ordos Basin China. Geology 44 (12), 1031–1034.

Zhang, W., Yang, W., Xie, L., 2017. Controls on organic matter accumulation in the Triassic Chang 7 lacustrine shale of the Ordos Basin, central China. Int. J. Coal Geol. 183, 38–51.

Zhao, X.H., Feng, X.S., 2014. Periodicities of solar activity and the surface temperature variation of the Earth and their correlations. Chinese Sci. Bull. 59 (14), 1284–1292.

Zhao, W.Z., Zhu, R.K., Hu, S.Y., Hou, L.H., Wu, S.T., 2020. Accumulation contribution differences between lacustrine organic-rich shales and mudstones and their significance in shale oil evaluation. Petroleum Explor. Dev. 47 (6), 1160–1171.

Zhou, D.W., Zhao, C.Y., Li, Y.D., Jian, W.C., Ye, J., Chen, G., 1995. Geological Features of Southwest Margin of Ordos Basin and Its Relationships with Qinling Orogenic Belt. Geological Publishing House, Beijing.

Zou, C.N., Zhu, R.K., Chen, Z.Q., Ogg, J.G., Wu, S.T., Dong, D.Z., Qiu, Z., Wang, Y.M., Wang, L., Lin, S.H., Cui, J.W., Su, L., Yang, Z., 2019. Organic-matter-rich shales of China. Earth-Sci. Rev. 189, 51–78.